

AD-A061 261

NAVAL RESEARCH LAB WASHINGTON D C

F/G 4/1

NONLINEAR EQUATORIAL SPREAD F: DEPENDENCE ON ALTITUDE OF THE F<sup>2</sup> --ETC(U)

APR 78 S L OSSAKOW, S T ZALESAK, B E MCDONALD

UNCLASSIFIED

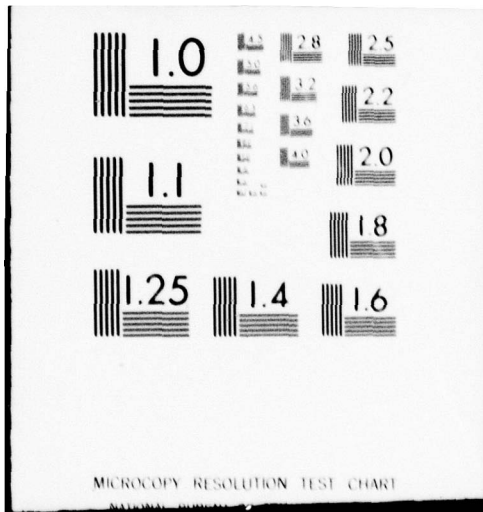
NRL-MR-3772

NL

1 OF 1  
AD  
A061 261



END  
DATE  
FILMED  
1-79  
DDC



MICROCOPY RESOLUTION TEST CHART

**LEVEL II**

**12**

NRL Memorandum Report 3772 *NW*

AD A061261

**Nonlinear Equatorial Spread F:  
Dependence on Altitude of the F Peak and  
Bottomside Background Electron  
Density Gradient Scale Length**

S. L. OSSAKOW, S. T. ZALESK, AND B. E. McDONALD

*Plasma Physics Division*

and

P. K. CHATURVEDI

University of Maryland  
College Park, Maryland 20742

April 1978

DDC FILE COPY

This research was sponsored in part by the Office of Naval Research and by the Defense Nuclear Agency under Subtask I25AAXYX960; Work Unit Code 11, Title "WB Scintillation Assessment."



DDC  
RECEIVED  
NOV 16 1978  
D

NAVAL RESEARCH LABORATORY  
Washington, D.C.

Approved for public release: distribution unlimited.

78 11 13 056

14 NRL-MR-3772

SECURITY CLASSIFICATION OF THIS PAGE (When Data Entered)

REPORT DOCUMENTATION PAGE		READ INSTRUCTIONS BEFORE COMPLETING FORM
1. REPORT NUMBER NRL Memorandum 3772	2. GOVT ACCESSION NO.	3. RECIPIENT'S CATALOG NUMBER 9
4. TITLE (and Subtitle) NONLINEAR EQUATORIAL SPREAD F: DEPENDENCE ON ALTITUDE OF THE F PEAK AND BOTTOMSIDE BACKGROUND ELECTRON DENSITY GRADIENT SCALE LENGTH	5. TYPE OF REPORT & PERIOD COVERED Interim report, in a continuing NRL Problem	
7. AUTHOR(s) S.L. Ossakow, S.T. Zalesak, B.E. McDonald P.K. Chaturvedi	8. CONTRACT OR GRANT NUMBER(s) 17 X960	
9. PERFORMING ORGANIZATION NAME AND ADDRESS Naval Research Laboratory Washington, D.C. 20375	10. PROGRAM ELEMENT, PROJECT, TASK AREA & WORK UNIT NUMBERS NRL Problem #H02-42D; A03-16B. DNA Subtask I25AAXYX960	
11. CONTROLLING OFFICE NAME AND ADDRESS Defense Nuclear Agency/Office of Naval Research Washington, D.C. 20305 Arlington, VA 22217	12. REPORT DATE 11 April 1978	13. NUMBER OF PAGES 64
14. MONITORING AGENCY NAME & ADDRESS (if different from Controlling Office) V2 65 p.	15. SECURITY CLASS. (of this report) UNCLASSIFIED	
16. DISTRIBUTION STATEMENT (of this Report) Approved for public release; distribution unlimited.		
17. DISTRIBUTION STATEMENT (of the abstract entered in Block 20, if different from Report)		
18. SUPPLEMENTARY NOTES This research was sponsored in part by the Office of Naval Research and by the Defense Nuclear Agency under Subtask I25AAXYX960; Work Unit Code 11, Title "WB Scintillation Assessment." *University of Maryland, College Park, MD 20742		
19. KEY WORDS (Continue on reverse side if necessary and identify by block number) Equatorial Spread F, Numerical Simulation, Collisional Rayleigh-Taylor Regime, Parameter dependence		
20. ABSTRACT (Continue on reverse side if necessary and identify by block number) Four different two dimensional (perpendicular to the ambient magnetic field), plasma fluid-type, numerical simulations following the nonlinear evolution of the collisional Rayleigh-Taylor instability in the nighttime equatorial F region ionosphere have been performed. Realistic altitude dependent ion-neutral collision frequencies, recombination rates, and ambient electron density profiles were used. In three cases (ESF 0, 1, 3) the electron density profile was kept constant, with a minimum bottomside background electron density gradient scale length $L \sim 10$ km, but the altitude of the F peak was changed, with F peak altitudes at 340, 350, and 430 km. All cases resulted in bottomside growth of the instability (Spread F) with dramatically different time scales about		

DD FORM 1 JAN 73 1473 EDITION OF 1 NOV 65 IS OBSOLETE S/N 0102-014-6601

SECURITY CLASSIFICATION OF THIS PAGE (When Data Entered)  
7.8 11 13 056  
251 950  
Gur

for development. Plasma density depletions were produced on the bottomside with rise velocities, produced by nonlinear polarization  $E \times B$  forces, of 2.5, 12, and 160 m/sec, and percentage depletions of 16, 40, and 85, respectively. In one case, ESF 0, the bubble did not rise to the topside, but in ESF 1 and 3 topside irregularities were produced by the bubbles (where linear theory predicts no irregularities.) In these three cases Spread F could be described from weak to strong. In the fourth case (ESF 2) the altitude of the F peak was 350 km, but the minimum L on the bottomside was changed to 5 km. This resulted in a bubble rise velocity  $\sim 23$  m/sec and a 60% depletion with strong bottomside and moderate topside Spread F and a time scale for development between ESF 1 and 3. Two other cases ESF 0' and 0'' with peaks at 330 and 300 km, respectively and bottomside L  $\sim 10$  km were investigated via linear theory. These cases resulted in extremely weak bottomside Spread F and no Spread F (entire bottomside linearly stable), respectively. These simulations show that, under appropriate conditions, the collisional Rayleigh-Taylor instability causes linear growth on the bottomside of the F region. This causes the formulation of plasma density depletions (bubbles) which rise to the topside (under appropriate conditions) F region by polarization  $E \times B$  motion. High altitude of the F peak, small bottomside electron density gradient scale lengths, and large percentage depletions yield large vertical bubble rise velocities, with the first two conditions favoring bottomside linear growth of the instability. The numerical simulation results are in good agreement with rocket and satellite in situ measurements and radar backscatter measurements, including some of the recent results from the August 1977 coordinated ground based measurement campaign conducted by DNA at Kwajalein.

**LEVEL II**

ACCESSION NO.	
DTIC	Write Section <input checked="" type="checkbox"/>
DDO	Soft Section <input type="checkbox"/>
UNANNOUNCED	<input type="checkbox"/>
JUSTIFICATION	
BY	
DISTRIBUTION/AVAILABILITY CODES	
NO.	AVAIL. CODE/IF SPECIAL
A	

DDC  
**RECEIVED**  
 NOV 16 1978  
**RECEIVED**  
 D

**CONTENTS**

**I. INTRODUCTION** ..... 1

**II. THEORY** ..... 2

**III. NUMERICAL RESULTS AND DISCUSSION** ..... 6

**IV. SUMMARY AND CONCLUSIONS** ..... 19

**Acknowledgement** ..... 24

**References** ..... 25

# NONLINEAR EQUATORIAL SPREAD F: DEPENDENCE ON ALTITUDE OF THE F PEAK AND BOTTOMSIDE BACKGROUND ELECTRON DENSITY GRADIENT SCALE LENGTH

## I. INTRODUCTION

In the past few years much effort has been expended to describe and explain equatorial Spread F phenomena both from an experimental and theoretical viewpoint (see for example: *Balsley et al.*, 1972; *Haerendel*, 1974; *Dyson et al.*, 1974; *Chaturvedi and Kaw*, 1975a,b; 1976; *Hudson and Kennel*, 1975; *Scannapieco and Ossakow*, 1976; *Kelley et al.*, 1976; *Woodman and La Hoz*, 1976; *Morse et al.*, 1977; *McClure et al.*, 1977; *Chaturvedi and Ossakow*, 1977; *Zalesak et al.*, 1977; *Szuszczewicz*, 1978; *Ott*, 1978; *Ossakow and Chaturvedi*, 1978; *Ossakow et al.*, 1978; *Hudson*, 1978; *Costa and Kelley*, 1978a,b; and *Kelley and Ott*, 1978). It is now generally believed that the collisional Rayleigh-Taylor instability (or possibly the  $\mathbf{E} \times \mathbf{B}$  gradient drift instability; in any case a fluid type gradient instability) initiates equatorial Spread F in the bottomside evening equatorial F region ionosphere (*Balsley et al.*, 1972; *Haerendel*, 1974; *Scannapieco and Ossakow*, 1976). Several recent experimental results lend credence to this idea (*Kelley et al.*, 1976; *Woodman and La Hoz*, 1976; *McClure et al.*, 1977). The generation of this instability on the bottomside leads to the formation of plasma density depletions (bubbles). These bubbles were predicted by the nonlinear numerical simulation studies (in the collisional Rayleigh-Taylor regime, denoted CR-T) of *Scannapieco and Ossakow* [1976] and have been observed experimentally (*Kelley et al.*, 1976; *Woodman and La Hoz*, 1976; *McClure et al.*, 1977).

The initial nonlinear numerical simulation studies (*Scannapieco and Ossakow*, 1976) showed how a plasma mode (CR-T), which is linearly unstable on the bottomside only, could,

by nonlinear polarization  $\mathbf{E} \times \mathbf{B}$  forces in the equatorial geometry, produce bubble induced irregularities on the topside, where the mode is linearly stable. In the present paper we give a more comprehensive derivation of the equations used by *Scannapieco and Ossakow (1976)* and extend the simulations in the CR-T regime by changing background ionospheric parameters. In particular, the altitude of the  $F$  peak is changed in different simulations, as is the bottomside background electron density gradient scale length. Both of these changes lead to important new simulation results. However, the most profound effect comes from changing the height of the  $F$  peak as this changes the effective ion-neutral collision frequency.

In section II the theory is presented; section III contains the numerical simulation results and discussion; and section IV gives the summary and conclusions.

## II. THEORY

In this section we present the two dimensional ( $x, y$ ; see Fig. 1) set of plasma fluid equations which are used to describe the nonlinear evolution of the collisional Rayleigh-Taylor (CR-T) instability for equatorial nighttime  $F$  region conditions. The ambient geomagnetic field,  $\mathbf{B}$ , is taken to be constant and in the  $z$  direction, the  $y$  axis is vertically upward (altitude), gravity,  $\mathbf{g}$ , is in the negative  $y$  direction, the  $x$  axis points westward, and  $\mathbf{g} \times \mathbf{B}$  is toward the east. The ambient electron density profile depicted in Fig. 1 shows a steep bottomside. The bottomside steepens due to recombination effects and electrodynamic forces. In what follows we will neglect any motions or variations parallel to  $\mathbf{B}$ . Consequently, all spatial derivatives will be taken in the  $x, y$  plane. The basic plasma two-fluid equations describing the system are

$$\frac{\partial n_\alpha}{\partial t} + \nabla \cdot (n_\alpha \mathbf{v}_\alpha) = -\nu_R (n_\alpha - n_{\alpha 0}) \quad (1)$$

$$\left( \frac{\partial}{\partial t} + \mathbf{v}_\alpha \cdot \nabla \right) \mathbf{v}_\alpha = \frac{q_\alpha}{m_\alpha} \left( \mathbf{E} + \frac{\mathbf{v}_\alpha \times \mathbf{B}}{c} \right) + \mathbf{g} - \nu_\alpha \mathbf{v}_\alpha \quad (2)$$

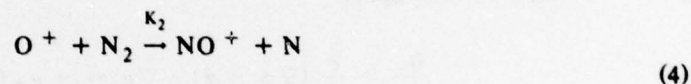
where the subscript  $\alpha$  denotes species ( $e$  is electron,  $i$  is ion),  $n$  is charged particle number den-

sity,  $\mathbf{v}$  is velocity;  $\nu_R$  is recombination rate;  $\mathbf{E}$  is the electric field;  $\mathbf{g}$  is gravity;  $q$  is the charge,  $\nu$  is collision frequency;  $c$  is the speed of light; and  $m$  is mass.

It should be noted that  $n_{\alpha 0}$  in Eq. (1) is the equilibrium value of the density such that in equilibrium the right hand side of Eq. (1) is zero. In the usual form the right hand side of Eq. (1) would have a source minus a loss. The loss term is represented by  $-\nu_R n_{\alpha}$  (Strobel and McElroy, 1970) and we have set the source term equal to  $\nu_R n_{\alpha 0}$  such that  $dn_{\alpha 0}/dt = 0$ . The recombination rate,  $\nu_R$ , represents a combination of the rate limiting charge exchange reaction



and the ion-molecule reaction



such that

$$\nu_R = K_1 n(\text{O}_2) + K_2 n(\text{N}_2) \quad (5)$$

where  $n(\text{O}_2)$  and  $n(\text{N}_2)$  are the neutral number densities of  $\text{O}_2$  and  $\text{N}_2$  respectively. In Eq. (2) the temperature and neutral wind have been set to zero (equivalently we are in a frame moving with the neutral wind).

Equation (2) is then solved for the electron and ion velocities as follows. The left hand side of Eq. (2), i.e., the inertial terms, are neglected so that the time changes associated with these terms occur over a time scale longer than the gyroperiod or collision time (equivalently the frequency associated with the inertial terms is small compared to the gyrofrequencies and collision frequencies). For the electrons we take  $\nu_e/\Omega_e = 0$ , where  $\Omega_{\alpha} = eB/m_{\alpha}c$  and for the ions  $\nu_i/\Omega_i \ll 1$ , where by  $\nu_i$  we mean ion-neutral collisions ( $\nu_{in}$ ). The equations for the electron and ion velocities are then given by

$$\mathbf{v}_e = \frac{c}{B} \mathbf{E} \times \hat{\mathbf{z}}, \quad \hat{\mathbf{z}} = \frac{\mathbf{B}}{|\mathbf{B}|} \quad (6)$$

$$\mathbf{v}_i = \left( \frac{\mathbf{g}}{\Omega_i} + \frac{c}{B} \mathbf{E} \right) \times \hat{\mathbf{z}} + \left( \frac{\mathbf{g}}{\Omega_i} + \frac{c}{B} \mathbf{E} \right) \frac{v_{in}}{\Omega_i} \quad (7)$$

where in (6) we have neglected the electron  $\mathbf{g} \times \hat{\mathbf{z}}$  motion, because compared with the same ion motion the ratio is  $m_e/m_i$ . Use is made of quasi-neutrality such that  $n_e = n_i = n$  and we use

$$\nabla \cdot \mathbf{J} = 0, \quad \mathbf{J} = en(\mathbf{v}_i - \mathbf{v}_e) \quad (8)$$

Eq. (8) can be obtained by subtracting the electron continuity equation from the ion continuity equation (Eq. (1) in the appropriate forms). The electrostatic approximation is made, i.e.,  $\mathbf{E} = -\nabla\phi$  and we then obtain

$$\frac{\partial n}{\partial t} - \frac{c}{B} (\nabla\phi \times \hat{\mathbf{z}}) \cdot \nabla n = -\nu_R (n - n_0) \quad (9)$$

$$\nabla \cdot (v_{in} n \nabla\phi) = \frac{m_i}{e} \mathbf{g} \cdot \nabla (v_{in} n) + \frac{B}{c} (\mathbf{g} \times \hat{\mathbf{z}}) \cdot \nabla n \quad (10)$$

Then we set  $\phi = \phi_0 + \phi_1$ , where  $\phi_0$  is the zero order potential and  $\phi_1$  is the induced or perturbed potential. The zero order solution of Eqs. (9) and (10) requires that  $\nabla\phi_0 = m_i \mathbf{g}/e$ . Note that this equilibrium value of the potential makes  $v_{i0} = 0$  (see Eq. (7)) and makes  $\mathbf{v}_{e0} = -(\mathbf{g} \times \hat{\mathbf{z}}/\Omega_i)$ . Thus the equilibrium current is carried by the electrons and we have  $\mathbf{J}_0 = -n_0 e \mathbf{g} \times \hat{\mathbf{z}}/\Omega_i$ . We then neglect any other zero order or ambient electric fields so that Eqs. (9) and (10) become

$$\frac{\partial n}{\partial t} - \frac{c}{B} (\nabla\phi_1 \times \hat{\mathbf{z}}) \cdot \nabla n = -\nu_R (n - n_0) \quad (11)$$

$$\nabla \cdot (v_{in} n \nabla\phi_1) = \frac{B}{c} (\mathbf{g} \times \hat{\mathbf{z}}) \cdot \nabla n \quad (12)$$

If  $\nu_{in}$  were constant then  $(B/c\nu_{in})(\mathbf{g} \times \hat{\mathbf{z}})$  would play the role of an effective electric field (see *Ossakow and Chaturvedi, 1978*) and  $-\nabla\phi_1$  is the induced or polarization electric field. Equations (11) and (12) are the basic equations we wish to solve for  $n$  and  $\phi_1$  in the  $x, y$  plane. In these equations  $n_o, \nu_{in}$ , and  $\nu_R$  are functions of  $y$  (altitude).

We may obtain the linear growth rate from Eqs. (11) and (12) by assuming that

$$\begin{aligned} n &= n_o(y) + n_1 e^{i(k_x x + k_y y - \omega t)} \\ \phi_1 &= \phi_1 e^{i(k_x x + k_y y - \omega t)} \end{aligned} \quad (13)$$

where we have made the local approximation  $k \gg (\partial n_o / \partial y)(1/n_o)$ . This results in the determinant set of equations

$$(-i\omega + \nu_R)n_1 + i \frac{c}{B} \frac{\partial n_o}{\partial y} k_x \phi_1 = 0 \quad (14)$$

$$\frac{B}{c} i k_x g n_1 + \left( \frac{\partial (n_o \nu_{in})}{\partial y} i k_y - n_o \nu_{in} k^2 \right) \phi_1 = 0 \quad (15)$$

This set yields

$$\omega = - \frac{i k_x^2 g \frac{\partial n_o}{\partial y}}{i k_y \frac{\partial (n_o \nu_{in})}{\partial y} - n_o \nu_{in} k^2} - i \nu_R \quad (16)$$

Setting  $\omega = \omega_r + i\gamma$  we obtain

$$\gamma = \frac{\frac{\partial n_o}{\partial y} k_x^2 g n_o \nu_{in} k^2}{(n_o \nu_{in} k^2)^2 + \left( k_y \frac{\partial (n_o \nu_{in})}{\partial y} \right)^2} - \nu_R \quad (17)$$

$$\omega_r = \frac{-k_x^2 k_y \frac{\partial (n_o \nu_{in})}{\partial y} g \frac{\partial n_o}{\partial y}}{(n_o \nu_{in} k^2)^2 + \left( k_y \frac{\partial (n_o \nu_{in})}{\partial y} \right)^2} \quad (18)$$

Equation (17) for the growth rate,  $\gamma$ , clearly shows that one can have growth (positive  $\gamma$ ) only on the bottomside of the  $F$  peak where  $\partial n_o/\partial y > 0$ . Moreover, growth (instability) occurs when the first term in (17) is greater than the second. Equation (17) clearly shows that on the topside where  $\partial n_o/\partial y < 0$   $\gamma$  is negative (stable). For purely horizontal propagating waves ( $k_y = 0$ ) the above discussion still applies and we obtain

$$\gamma = \frac{1}{n_o} \frac{\partial n_o}{\partial y} \frac{g}{v_{in}} - \nu_R \quad (19)$$

$$\omega_r = 0 \quad (20)$$

and we can identify  $n_o (\partial n_o/\partial y)^{-1}$  with the background electron density gradient scale length  $L$ . In the denominator of Eqs. (17) and (18) the second term is small compared with the first if  $kL \gg 1$  (neglecting the  $\nu_{in}$  altitude dependence) which is just the local approximation. Then Eqs. (17) and (18) become

$$\gamma = \frac{1}{n_o} \frac{\partial n_o}{\partial y} \frac{k_x^2}{k^2} \frac{g}{v_{in}} - \nu_R \quad (21)$$

$$\omega_r = - \frac{k_x^2 k_y g \frac{\partial n_o}{\partial y} \frac{\partial (n_o \nu_{in})}{\partial y}}{(n_o \nu_{in} k^2)^2} \quad (22)$$

Equation (21) shows that the growth rate is independent of  $|k|$  and maximizes when  $k^2 = k_x^2$  (horizontal propagation). Also if one neglects the  $y$  dependence of  $\nu_{in}$  then (22) shows that  $\omega_r \sim - (g/\nu_{in}L) (1/kL)$  or  $-(kL)^{-1}$  times the growth rate.

### III. NUMERICAL RESULTS AND DISCUSSION

The basic equations to be solved are (11) and (12). Equation (11) is put into dimensionless form with  $Q \equiv n/n_o$ . Equation (11) then becomes

$$\begin{aligned} & \left. \frac{\partial Q}{\partial t} - \frac{c}{B} \left[ \frac{\partial}{\partial x} \left( Q \frac{\partial}{\partial y} \phi_1 \right) - \frac{\partial}{\partial y} \left( Q \frac{\partial}{\partial x} \phi_1 \right) \right] \right\} \\ & = - \frac{c}{B} \frac{Q}{n_o} \frac{\partial n_o}{\partial y} \frac{\partial \phi_1}{\partial x} - \nu_R (Q - 1) \end{aligned} \quad (23)$$

where we have used  $\partial n_o / \partial t = 0$ . Equation (12) becomes

$$\begin{aligned} & \frac{\partial^2 \phi_1}{\partial x^2} + \frac{\partial^2 \phi_1}{\partial y^2} + \left( \frac{1}{\nu_{in}} \frac{\partial \nu_{in}}{\partial y} + \frac{1}{Q} \frac{\partial Q}{\partial y} + \frac{1}{n_o} \frac{\partial n_o}{\partial y} \right) \frac{\partial \phi_1}{\partial y} \\ & + \frac{1}{Q} \frac{\partial Q}{\partial x} \frac{\partial \phi_1}{\partial x} = - \frac{B}{c} \frac{g}{\nu_{in}} \frac{1}{Q} \frac{\partial Q}{\partial x}. \end{aligned} \quad (24)$$

In Eqs. (23) and (24)  $\nu_{in}$  and  $\nu_R$  are functions of altitude ( $y$ ). The ion-neutral collision frequency,  $\nu_{in}$ , is given by (Strobel and McElroy, 1970)

$$\nu_{in} = 2.4 \times 10^{-11} \sqrt{T} n_n \quad (25)$$

where  $n_n$  is the neutral density in  $\text{cm}^{-3}$ , and  $T$  is the atmospheric temperature in  $^\circ\text{K}$ . Equation (25) represents the collision frequency for  $\text{O}^+$  in  $\text{O}$ . The recombination rate,  $\nu_R$ , is given by Eq. (5) with (McFarland et al., 1973)

$$K_1 = 2 \times 10^{-11} \left( \frac{300}{T} \right)^{0.4} \quad (26)$$

$$K_2 = \begin{cases} 1.2 \times 10^{-12} \left( \frac{300}{T} \right), & T \leq 750^\circ \text{K} \\ 8 \times 10^{-14} \left( \frac{T}{300} \right)^2, & T > 750^\circ \text{K} \end{cases} \quad (27)$$

The atmospheric quantities in Eqs. (5), (25), (26) and (27) were obtained from a Jacchia 1965 model neutral atmosphere. Both  $\nu_{in}$  and  $\nu_R$  used in the numerical simulations are depicted in Fig. 2.

The results of four nonlinear numerical simulations will be presented. The simulations are listed in Table 1 and the differences in the ambient zero order driving conditions are clearly delineated. For these equatorial spread F (ESF) cases only those parameters listed in the table were changed. All other conditions were the same from simulation to simulation. ESF 1 is taken to be the canonical case because it has essentially the original simulation conditions of *Scannapieco and Ossakow (1976)*. In ESF O we have taken the  $n_o(y)$  profile of ESF 1 and moved it down 10 km, i.e., the shape is the same but the  $n_o$  at any altitude changes (see Figs. 5 and 11). Similarly in ESF 3 the profile of ESF 1 is moved up 80 km (see Figs. 5 and 9). In ESF 2 in the region of maximum growth rate of ESF 1 the bottomside ambient electron density gradient scale length has been made smaller, i.e., the bottomside profile is steeper, (see Figs. 5 and 7). The linear growth rates for these four cases are plotted in Fig. 3. For completeness, linear damping rates for two other cases ESF O' and ESF O'' are displayed in Fig. 4. ESF O' is the same profile as ESF 1 with the F peak moved down 20 km. ESF O'' is also the same profile as ESF 1, but with the peak moved down 50 km. In arriving at the curves in Figs. 3 and 4, a horizontal perturbation was assumed, i.e.,  $n_1, \phi_1 \propto \exp[i(k_x x - \omega t)]$  and use was made of Eq. (19) with  $\nu_{in}$  and  $\nu_R$  as given in Fig. 2.

All four nonlinear numerical simulations were performed over a two dimensional mesh corresponding to an altitude ( $y$ ) range of 200 km, i.e., the highest  $y$  point minus the lowest  $y$  point was 200 km, and an east-west ( $x$ ) extent of 8 km (see Figs. 5, 7, 9 and 11). The mesh was such that there were 102 points in the  $y$  direction and 42 points in the  $x$  direction and periodic boundary conditions in both directions. This corresponds to  $\Delta y = 2$  km and  $\Delta x = 200$  meters. Equation (23) was integrated forward in time using flux-corrected transport algorithms (*Boris and Book, 1973*), while Eq. (24) was solved using a Chebychev-iterative relaxation technique (*McDonald, 1977*). The background zero order ionospheric electron density,  $n_o$ , em-

ployed in each simulation is depicted in Figs. 5, 7, 9 and 11. Superimposed on the background density at  $t = 0$  was an initial cosinelike perturbation (the same for each simulation) of the form (applied over the entire mesh),

$$\frac{n_1}{n_0} - Q - 1 = -e^{-3} \begin{cases} \cos\left(\frac{\pi x}{1.6}\right), & 0 \leq |x| \leq 1.6 \text{ km} \\ \frac{1}{2} \left[ \cos\left(\frac{\pi x}{1.6}\right) - 1 \right], & 1.6 \leq |x| \leq 3.2 \text{ km} \\ 0, & |x| > 3.2 \text{ km} \end{cases} \quad (28)$$

where  $x$  is in km and  $x = 0$  is in the center of the  $x$  mesh (see Figs. 5, 7, 9 and 11).

*ESF 1 Case.* The  $n_0$  profile used in this canonical case is depicted in Fig. 5. The  $y$  extent of the mesh runs from 252 km to 452 km with the F peak at 354 km. The shortest bottomside background electron density gradient scale lengths  $L = n_0 (\partial n_0 / \partial y)^{-1}$  are  $\sim 10$  km and essentially occur in the range 252 to 298 km. The largest linear growth rate (see Fig. 3),  $\gamma_M = 1.01 \times 10^{-3} \text{ sec}^{-1}$  and occurs at an altitude of 298 km. At this altitude  $\nu_R = 3.7 \times 10^{-4} \text{ sec}^{-1}$ . Figure 3 depicts the range of linear instability for ESF 1 and this is from 274 to 350 km in altitude. Below 274 km  $L$  is small, but recombination prevails (see Fig. 2) and between 350 and 354 km  $L$  is large and recombination prevails. Exactly at the F peak (354 km),  $\partial n_0 / \partial y = 0$ , i.e.,  $L = \infty$ , and  $\gamma = -\nu_R$  (see Eq. (19)). Of course above 354 km (the F peak in this case), the gradient changes sign and all perturbations are linearly stable. Note in Fig. 3 that for all cases we have plotted only the regions of instability (growth), i.e., positive  $\gamma$ . Between 274 km and 298 km  $\gamma$  goes from  $4.4 \times 10^{-5} \text{ sec}^{-1}$  to  $1.01 \times 10^{-3} \text{ sec}^{-1}$  and  $\nu_R$  goes from  $7.98 \times 10^{-4}$  to  $3.73 \times 10^{-4} \text{ sec}^{-1}$ . Between 298 km and 350 km,  $\gamma$  goes from  $1.01 \times 10^{-3} \text{ sec}^{-1}$  to  $3.48 \times 10^{-5} \text{ sec}^{-1}$  and  $\nu_R$  at 350 km is  $7.47 \times 10^{-5} \text{ sec}^{-1}$ .

Figure 5 exhibits contour plots of constant  $n/n_0$  or equivalently  $n_1/n_0$ , at  $t = 2000, 4000, 8000,$  and  $10,000$  sec in the development of ESF 1. Each is overlaid with a plot of  $n_0$  (large dashed curve) as a function of altitude. At  $t = 2000$  sec the early phase of the growth of the collisional Rayleigh-Taylor instability is exhibited. It shows the formation of plasma density enhancements (+) and depletions (-), depicted by small dashed and solid contours, respectively. The depletion contour represents a 16% depletion, with a maximum depletion of 27% within this contour; whereas, the enhancement contour represents a 19% enhancement, with a maximum enhancement of 23% within this contour. Here and in subsequent Figures 7, 9, and 11 the contour plotting is such that the first (outer) depletion contour  $n/n_0$  is  $2^{-1/4}$  and each succeeding inner contour is  $2^{-1/2}$  times the previous one. Then we subtract 1.0 to find  $n_1/n_0$  for depletions. For example, for three depletion contours, the outermost would have  $n_1/n_0 = 0.84$  (16% depletion), the next inner one  $n_1/n_0 = 0.59$  (41% depletion), and the innermost  $n_1/n_0 = 0.42$  (58% depletion). For the enhancement contours, the first outer contour is  $2^{1/4}$  and the succeeding inner ones are  $2^{1/2}$  times the previous ones. Then, we subtract 1.0 to obtain  $n_1/n_0$  for enhancements. For example, for three enhancement contours, the outermost would have  $n_1/n_0 = 1.19$  (19% enhancement), the next inner one  $n_1/n_0 = 1.68$  (68% enhancement), and the innermost  $n_1/n_0 = 2.38$  (138% enhancement). With this scheme, for the depletions (enhancements) every other contour of  $n_1/n_0$  is a factor of two smaller (larger).

At  $t = 4,000$  sec, in Fig. 5, a clear bubble (density depletion) in the center of the  $x$  direction is beginning to form and rise toward the F peak with an innermost depletion contour of 41% with a maximum depletion within this contour of 54%. The innermost enhancement contour is 68%, with a maximum enhancement of 84% within this contour. We also note the formation of other depletions in the wings (near  $|x| \sim 4$  km). At  $t = 8000$  sec, the density depletion or bubble upper boundary is at the F peak. The innermost contour of the rising bubble is a 41% depletion; however, there is a 58% depletion contour below this at an altitude  $\sim 300$  km and within this contour a maximum depletion of 66%. In the wings there are depletions with

innermost contours of 71% depletion. There are plasma density enhancements at  $y \leq 302$  km with innermost contours of 138% enhancements and maximum enhancements inside these innermost contours of 226%.

At  $t = 10,000$  sec (as far as the ESF 1 simulation was carried), the main bubble is clearly through the F peak with an innermost depletion contour of 41%. However, in the ionosphere below the bubble near  $x = 0$ , there is a 71% depletion contour with a maximum depletion inside this contour of 73%. In the wings there are depletions with innermost contours of 71% and inside of these depletion contours maximum depletions of 75%. The innermost enhancement contour is 236% with a maximum inside this contour of 294%.

Although there is a main bubble which is beyond the F peak (top of bubble at 375 km) at this time, it has not completely broken from the lower altitude region and is forming a trailing tail. The top of the main bubble in the central  $x$  region is at an altitude  $\sim 375$  km with the bottom of the trail at an altitude  $\sim 270$  km. The widest part of the top outermost contour (16% depletion) of the bubble is  $\sim 3$  km, whereas; the innermost contour (41% depletion) is  $\sim 0.5$  km wide. Also from  $t = 8,000$  to  $t = 10^4$  sec in Fig. 5, the top most part of the bubble has moved  $\sim 24$  km which corresponds to a rise velocity  $\sim 12$  m/sec. At this time the enhanced regions encompass a large region in the east-west ( $x$ ) direction although confined in altitudes  $\leq 320$  km (basically isolated depletions move upward, while isolated enhancements move downward in the equatorial spread F geometry; see *Ossakow and Chaturvedi, 1978*).

Figure 6 displays contours of constant induced potential  $\phi_1$ , from Eq. (24), for ESF 1 over the computational mesh at  $t = 10^4$  sec. The plus (inside solid lines) denotes positive values and the minus (inside dashed lines) denotes negative values of potential. Zero potential falls between the two in such a way that the outermost solid contour represents a potential of  $5 \times 10^{-4}$  statvolts (0.15 volts) and the outermost dashed contour represents a potential of

$-5 \times 10^{-4}$  statvolts. Each inner solid contour represents an increment of  $5 \times 10^{-4}$  statvolts and similarly each inner dashed contour represents an increment of  $-5 \times 10^{-4}$  statvolts. Consequently, the potential difference between any two solid (dashed) contours is  $5 \times 10^{-4}$  ( $-5 \times 10^{-4}$ ) statvolts. However, the potential difference between the outermost solid and dashed contours is  $10^{-3}$  statvolts (0.3 volts). This contour level scheme is the same in Figs. 8 and 10. We see that the more isolated high altitude part of the central bubble is acted on by an induced electric field which points from west (positive  $x$ ) to east (negative  $x$ ) and is dipolar in nature. This causes the bubble to rise with a velocity  $(-c/B)\nabla\phi_1 \times \hat{z}$ . However, the lower portion of the mesh is acted on by an induced electric field which points from east to west and is much weaker than the induced electric field acting upon the isolated portion of the central bubble. This basically causes the enhancements to move downward along with the lower altitude depletions. Thus the lower part of the central bubble becomes "captured" by the enhancements. As stated previously isolated depletions and enhancements should move up and down respectively, at the equator. However, this concept is altered when depletions are surrounded by enhancements or vice versa.

*ESF 2 Case.* The  $n_o$  profile used in this case is displayed in Fig. 7. The  $y$  extent is the same as ESF 1 with the F peak at 354 km. However, in this case the bottomside is steeper than ESF 1 and the shortest bottomside background electron density gradient scale lengths  $L$  are  $\sim 4.8$  km and occur in the altitude range between 296 and 304 km. The largest linear growth rate (see Fig. 3),  $\gamma_M = 3.2 \times 10^{-3} \text{ sec}^{-1}$  (a factor of three larger than ESF 1) and occurs at an altitude of 304 km. At this altitude  $\nu_R = 3.09 \times 10^{-4} \text{ sec}^{-1}$ . The range of linear instability for ESF 2 is depicted in Fig. 3. This goes from 282 km to 352 km in altitude. At the lowest altitudes  $n_o$  is approximately the same for ESF 1 and 2. This makes  $L$  larger at lower altitudes for ESF 2. Consequently, while ESF 1 is linearly unstable down to an altitude of

274 km, ESF 2 is unstable only down to 282 km. Between 282 and 304 km  $\gamma$  goes from  $4.5 \times 10^{-5} \text{ sec}^{-1}$  to  $3.2 \times 10^{-3} \text{ sec}^{-1}$  and  $\nu_R$  goes from  $6.19 \times 10^{-4} \text{ sec}^{-1}$  to  $3.09 \times 10^{-4} \text{ sec}^{-1}$ . Between 306 km and 352 km,  $\gamma$  goes from  $2 \times 10^{-3} \text{ sec}^{-1}$  to  $6.82 \times 10^{-5} \text{ sec}^{-1}$  and  $\nu_R$  at 352 km is  $7.02 \times 10^{-5} \text{ sec}^{-1}$ .

Figure 7 shows contour plots of constant  $n/n_0$  (or  $n_1/n_0$ ) at  $t = 1000, 3000, 4000,$  and  $5000 \text{ sec}$  in the nonlinear development of ESF 2. Also depicted in each snapshot in this figure is a plot of  $n_0$  as a function of altitude for this simulation. At  $t = 1000 \text{ sec}$  the innermost depletion contour represents a 58% depletion with a maximum depletion inside this contour of 60%. The enhancement contour represents a 19% enhancement. However, because of the enhancement contour spacings, there exists a 63% maximum enhancement inside the enhancement contour. This first frame clearly shows that ESF 2 is developing faster than ESF 1. At  $t = 3000 \text{ sec}$  the bubble is clearly rising toward the F peak. In the upper part of the bubble, near 340 km, the innermost depletion contour represents a 71% depletion. However, a maximum depletion of 82% occurs in the lower portion of the bubble, near 315 km, inside the 79% depletion contour. At this time the enhancement contours are much more widespread than in the case of ESF 1 with a maximum enhancement of 2490%. These enhancements are confined in altitude with  $280 \text{ km} \leq y \leq 305 \text{ km}$ . At  $t = 4000 \text{ sec}$  the main part of the bubble is already past the peak. In the upper part of the bubble the innermost depletion contour is 58%; however, a maximum depletion of 68% occurs inside the third (innermost) depletion contour at lower ( $\sim 320 \text{ km}$ ) altitudes, i.e., within the trail. Some well defined depletions (bubbles) are also evident in the lower regions ( $\sim 310 \text{ km}$  altitude) to the east and west of the main bubble ( $|x| \sim 2 \text{ km}$ ). Also at this time there are large regions of enhancements confined to altitudes  $275 \text{ km} \leq y \leq 310 \text{ km}$  with maximum enhancements of 2936%.

At  $t = 5000 \text{ sec}$  (as far as ESF 2 was run), the bubble clearly is well past the F peak leaving a trail in the lower ionosphere. However, the trail is not as well captured as in ESF 1. The

bubble and trail here extend for about 100 km in altitude as was the case in ESF 1. The innermost contour of the high altitude part of the bubble (top of bubble at 387 km altitude) is now only 41% and there is a maximum depletion of 73% in the lower portion of the bubble, near 325 km, within the 71% depletion contour. The widest part of the 16% depletion contour near the top of the bubble is  $\sim 3$  km; whereas, the 41% depletion (inner) contour is  $\sim 0.5$  km wide. Between  $t = 3000$  and  $4000$  sec the top of the bubble has moved up  $\sim 23$  km which corresponds to a rise velocity  $\sim 23$  m/sec. There is a slight rise in the bubbles to the east and west of the main bubble (compare with  $t = 4000$  sec). The enhancements are confined between  $275 \text{ km} \leq y \leq 310 \text{ km}$  with a maximum enhancement of 3130%.

Figure 8 depicts contours of constant induced potential  $\phi_1$  for ESF 2 over the computational mesh at  $t = 5000$  sec. The contours have the same scheme as for ESF 1. Once again this figure shows that the more isolated high altitude part of the bubble is acted upon by an induced polarization electric field which points from west to east and is somewhat dipolar in nature. This field is stronger than in the case of ESF 1 (see Fig. 6; note that in ESF 2 there are more potential contours and the spacing between the outermost negative contour and outermost positive contour is closer for ESF 2 than ESF 1) and accounts for the more rapid rise (through  $-(c/B) \nabla \phi_1 \times \hat{z}$ ). The lower portion of the mesh, like ESF 1, is acted upon by an induced electric field which points from east to west and is much weaker than the induced electric field which acts on the isolated portion of the central bubble. This field keeps the lower portion containing enhancements and depletions at low altitudes.

*ESF 3 Case.* Displayed in Fig. 9 is the  $n_o$  profile used in this case. The  $y$  extent is now between 332 km and 532 km with the F peak at 434 km. This F peak is 80 km higher than ESF 1 and is about at the altitude that Kelley et al. [1976] measured the F peak after encountering a bubble below the peak. The basic shape of the profile is the same as ESF 1 so

that the shortest bottomside background electron density gradient scale lengths  $L \sim 10$  km and occur in the altitude range between 332 km and 378 km (note this is just 80 km higher than ESF 1). The largest linear growth rate (see Fig. 3),  $\gamma_M = 6.07 \times 10^{-3} \text{ sec}^{-1}$  and occurs at an altitude of 378 km where  $\nu_R = 3.2 \times 10^{-5} \text{ sec}^{-1}$ . This linear growth rate is a factor of six larger than the maximum growth rate in ESF 1. Unlike ESF 1 or 2, in ESF 3 the entire bottomside is linearly unstable. Between 332 km and 432 km the recombination term in Eq. (19) does not balance the gradient term. In this altitude range  $\nu_R$  goes from  $1.3 \times 10^{-4} \text{ sec}^{-1}$  to  $6.4 \times 10^{-6} \text{ sec}^{-1}$  while  $\gamma$  goes from  $2.5 \times 10^{-3} \text{ sec}^{-1}$  to  $1 \times 10^{-4} \text{ sec}^{-1}$ . We also note again at the F peak, 434 km,  $L = \infty$  and there is damping of the instability.

Figure 9 displays contour plots of constant  $n/n_o$  (or  $n_1/n_o$ ) at  $t = 300, 700, 1000,$  and  $1400$  sec in the nonlinear evolution of ESF 3. Once again  $n_o$  as a function of altitude for this simulation is depicted in each of the frames. At  $t = 300$  sec the early phase is exhibited with a 16% depletion contour with a maximum depletion inside this contour of 26%. The enhancement contour represents a 19% enhancement with a maximum 23% enhancement inside this contour. Clearly this simulation is developing more rapidly than either ESF 1 or 2. At  $t = 700$  sec a rising bubble in the central  $x$  region is forming with an innermost depletion contour of 79%, with a maximum depletion inside this contour of 84%. Depletion contours of 16% in the wings are also in evidence. The innermost enhancement contour represents a 138% enhancement with a 187% enhancement maximum inside this contour. At  $t = 1000$  sec we see the bubble rising past the F region peak. At this time the innermost depletion contour, in the high altitude portion of the bubble (near 430 km), represents an 85% depletion and there is a maximum depletion inside this contour of 85.2%. There is a long trail associated with the bubble at this time which extends about 100 km in altitude. However, the trail is not as well captured as in ESF 1. The depletions in the wings, near  $|x| \sim 4$  km, exhibit an innermost contour of 58%

depletion. The enhanced regions at this time show an innermost contour of 572% enhancement with a maximum enhancement of 674% inside of this contour. Here we also note that the enhancements encompass a sizeable region in the  $x$  direction, but are confined to altitudes  $\leq 390$  km.

At  $t = 1400$  sec (as far as ESF 3 was carried), the top of the main bubble in the central  $x$  region is at an altitude  $\sim 500$  km which is well beyond the  $F$  peak altitude of 434 km. Moreover, this bubble has a long trail connecting it to an altitude of 357 km. The widest part of the top outermost 16% depletion contour is  $\sim 3$  km; whereas, the innermost 58% depletion contour is  $\sim 0.5$  km wide. Therefore, this shows a long narrow bubble which extends  $\sim 150$  km in altitude and a few km in the east-west dimension. Radar backscatter observations (Woodman and La Hoz, 1976) have exhibited, on occasion, "plumes" to extend over 100 km in altitude. They have identified these plumes with regions of depleted plasma density. Within the innermost bubble contour at high altitudes, in Fig. 9 at 1400 sec, there is a maximum depletion of 70%. The innermost contour in the depleted wings represents a 96% depletion with a maximum depletion inside this contour of 97%. The innermost contour in the enhancement region corresponds to a 2590% enhancement with a maximum enhancement of 2640% inside this contour. Between  $t = 1000$  sec and 1400 sec the top part of the bubble rose  $\sim 65$  km and this represents a rise velocity  $\sim 160$  m/sec. This is large compared with the 12 m/sec of ESF 1 and the 23 m/sec of ESF 2.

Figure 10 depicts contours of constant induced potential,  $\phi_1$ , over the ESF 3 computational mesh at  $t = 1400$  sec. Once again the more isolated high altitude part of the central bubble (see Fig. 9) is acted on by a dipolar like induced electric field pointing from west to east. This causes the bubble to rise with the  $-(c/B)\nabla\phi_1 \times \hat{z}$  velocity. The outermost positive and negative potential contours are more closely spaced than in either ESF 1 or 2 and results

in a more rapid rise velocity. The lower portion of the mesh is acted on by an induced electric field which points from east to west and this is much weaker than the higher altitude electric field pointing from west to east. This causes the low altitude enhancements and depletions to remain at low altitudes and results in a capturing of the central portion of the rising bubble.

*ESF O Case.* Figure 11 depicts the  $n_o$  profile used in this simulation. The  $y$  extent is now between 242 km and 442 km with the  $F$  peak at 344 km. This is the same shape profile as ESF 1 except that the profile has been moved down 10 km. Consequently, the shortest bottomside background electron density gradient scale lengths  $L \sim 10$  km and occur in the altitude range between 242 km and 288 km. The largest linear growth rate (see Fig. 3),  $\gamma_M = 6.18 \times 10^{-4} \text{ sec}^{-1}$  and occurs at an altitude of 288 km where  $\nu_R = 5.12 \times 10^{-4} \text{ sec}^{-1}$ . This linear growth rate is about 60% of the ESF 1 maximum linear growth rate. From Fig. 3 we note that the ESF O and ESF 1 growth rates are the same up to 288 km and both are stable below 274 km. In Fig. 3, ESF O shows instability between 274 km and 332 km. This is over a narrower altitude range than either ESF 1, 2, or 3 and represents weak instability. In this altitude range  $\gamma$  goes from  $4.55 \times 10^{-5} \text{ sec}^{-1}$  to  $3.94 \times 10^{-5} \text{ sec}^{-1}$  and  $\nu_R$  goes from  $7.98 \times 10^{-4} \text{ sec}^{-1}$  to  $1.3 \times 10^{-4} \text{ sec}^{-1}$ .

Figure 11 depicts contour plots of constant  $n/n_o$  (or  $n_1/n_o$ ) at  $t = 5000, 10,000$  and  $15,000$  sec. At  $t = 5000$  sec there is a 16% depletion contour with a maximum depletion inside this contour of 33%. There is a 19% enhancement contour with a maximum enhancement of 33% inside this contour. This shows a much slower development than ESF 1. At  $t = 10,000$  sec a central bubble, disconnected from the lower depletion, appears to be rising toward the  $F$  peak. The depletion contour of this bubble is 16% with a maximum depletion of 24% inside this contour. There are 16% depletion contours in the wings at 290 km altitude near  $|x| = 4$  km which have 37% maximum depletions inside of them. There is also a wide 19% enhancement contour with maximum enhancements inside the contour of 58%.

At  $t = 15,000$  sec the bubble has risen very slowly and appears to be drying up. At this time the top of the rising bubble is at an altitude of 320 km and has the 16% depletion contour as at  $t = 10,000$  sec, except over a smaller area. There is a maximum depletion of 29% inside the lower bubble (near 283 km) which also has a 16% depletion contour. In the wings, near 290 km altitude, there are 41% depletion contours with maximum depletions inside these contours of 44%. Inside the 19% enhancement contour is a maximum enhancement of 43%. In going from  $t = 10,000$  sec to 15,000 sec both enhancements and depletions appear to be decaying, even though the main bubble is rising. At an altitude of 320 km  $\nu_R^{-1} \sim 5000$  sec. Consequently, in this ESF O case, recombination plays a great role, especially considering the fact that the linear growth rates are not very large. Between 10,000 and 15,000 sec the top of the rising bubble has moved 12.5 km. This corresponds to a vertical rise velocity of 2.5 m/sec. Moreover, this 16% depletion contour in this rising bubble is  $\sim 0.7$  km wide and is  $\sim 6$  km long in the altitude direction. For ESF O, the enhancements and depletions are weak and, for the most part, reside in an altitude layer where  $268 \text{ km} \leq y \leq 300 \text{ km}$  (bottomside). In this layer, the bottomside gradient is sharp. This type of Spread F condition, i.e., ESF O, could correspond to the weak bottomside Spread F identified by *Woodman and La Hoz* [1976].

*ESF O' and ESF O'' Cases.* Although we have not performed numerical simulations for these two cases, we can estimate the effects based on the four simulations presented. For ESF O', the  $n_o$  profile of ESF 1 was moved down 20 km, i.e., the F peak was at 334 km (10 km lower than ESF O). Here the shortest bottomside electron density gradient scale lengths,  $L \sim 10$  km and occur over an altitude range between 232 km and 278 km. For this case there is a very narrow region between 274 km and 280 km where linear instability occurs (see Fig. 4). The maximum growth rate,  $\gamma_M$ , is  $2.15 \times 10^{-4} \text{ sec}^{-1}$  and occurs at an altitude of 278 km. This is almost an order of magnitude smaller growth rate than ESF 1 and one-third the growth rate of ESF O. From 232 km to 272 km the damping rate  $-\gamma$  goes from  $2.82 \times 10^{-3} \text{ sec}^{-1}$

to  $4.26 \times 10^{-5} \text{ sec}^{-1}$  (see Fig. 4). From 282 km to 432 km the damping rate goes from  $2.27 \times 10^{-4} \text{ sec}^{-1}$  to  $1.27 \times 10^{-3} \text{ sec}^{-1}$  (also see Fig. 4). In ESF O there was a 60 km region of linear instability (growth) and here there is only a 6 km region of instability with smaller growth rates. Consequently, the time scale for development here would be even longer and the strength even smaller. Consequently, we would expect extremely weak spread F for ESF O'.

In the case of ESF O" the  $n_o$  profile of ESF 1 was moved down 50 km, i.e., the F peak was lowered to 304 km. Consequently, the shortest L  $\sim 10$  km are in the range from 202 km to 248 km. However, in the entire range from 202 km to 402 km altitude, there is no linear instability. In this range the damping rate (see Fig. 4) goes from  $8.75 \times 10^{-3} \text{ sec}^{-1}$  to  $7.87 \times 10^{-4} \text{ sec}^{-1}$ . Consequently, no spread F would occur for this case ESF O".

#### IV. SUMMARY AND CONCLUSIONS

We have presented the results of four nonlinear numerical simulations of the collisional Rayleigh-Taylor instability for equatorial spread F geometry, using realistic altitude profiles for ion-neutral collision frequency, recombination rates and background electron density, in section III. Two other cases where the altitude of the F peak was lowered with respect to our canonical case ESF 1 were investigated via linear theory and conclusions were drawn based on the four numerical simulations. A summary of these results is presented in Table 2. We find that under favorable conditions, e.g., high altitude of the F peak (small effective ion-neutral collision frequency) and/or steep bottomside background electron density gradients, the collisional Rayleigh-Taylor instability causes linear growth on the bottomside of the F region. This in turn causes plasma density depletions or bubbles to be formed on the bottomside which then steepen on their top (see *Ossakow and Chaturvedi, 1978*) and nonlinearly rise to the topside by polarization (induced)  $\mathbf{E} \times \mathbf{B}$  motion. This produces irregularities on the topside

where a linear analysis would predict no irregularities. High altitude of the F peak ( $h_p$ ; see Table 2, ESF 3), small bottomside background electron density gradient scale lengths ( $L$ ; see Table 2, ESF 2), and large percentage depletions ( $n_1/n_0$ ) yield large vertical bubble rise velocities,  $V_B$ . Indeed, we have shown (see Table 2 and Section III) that changing the altitude of the F peak from 300 km to 430 km can have dramatic effects on the evolution of equatorial Spread F.

With relation to analytic studies of rising constant density, constant shape isolated equatorial Spread F bubbles in the collisional Rayleigh-Taylor regime, *Ossakow and Chaturvedi* [1978] have shown that the rise velocity is given by

$$V_B = \frac{g}{v_{in}} \frac{\frac{a}{b} \frac{n_1}{n_0}}{1 + \frac{a}{b} \left(1 - \frac{n_1}{n_0}\right)} \quad (29)$$

where  $a$  is one axis of the ellipse in the direction of  $\mathbf{g}$ ,  $b$  is the other axis in the east-west direction, and  $n_1/n_0$  here is the fractional density depletion (a positive number in this formula). Applying Eq. (29) to the bubble velocities and  $n_1/n_0$  in Table 2, along with the appropriate value of  $v_{in}$  (Fig. 2), we find that for ESF 0, 1, 2, and 3  $1 \lesssim a/b \lesssim 2$ . This shows that in trying to model a steepening bubble, which has a density distribution inside of it, with a constant density-constant shaped bubble results in the preference of circular-like shapes. Furthermore, the greater bubble velocity of ESF 3 over ESF 1 can be understood as follows. Equation (29) and the general results of *Ossakow and Chaturvedi* [1978] show for the collisional Rayleigh-Taylor regime

$$V_B = \frac{g}{v_{in}} f(n_1/n_0) \quad (30)$$

where  $f(n_1/n_0)$  is an increasing function of the fractional depletion  $n_1/n_0$  and depends on bubble shape. Raising the altitude of the F peak (as in ESF 3) decreases  $\nu_{in}$ . Also in the ESF 3 simulation  $n_1/n_0$  is larger (see Table 2) and both factors tend to increase  $V_B$ . Furthermore,  $n_1/n_0$  is predicted to be larger in ESF 3 over ESF 1, at least according to linear theory, because  $n_1 \propto \exp \gamma t$  where  $\gamma \propto \nu_{in}^{-1}$  and is given by Eq. (19). Raising the height of the F peak increases the growth rate,  $\gamma$ . Thus, the ion-neutral collision frequency,  $\nu_{in}$ , enters in two places in Eq. (30); whereas, the bottomside background scale length,  $L$  enters only in  $f$  (at least by the above argument). Similar arguments can be made in comparing ESF 0 and 2 with ESF 1.

To be sure we have not included a horizontal ambient zero order electric field,  $E_o$ , in the problem. Inclusion of such a field would in the  $E_o \times B$  drift frame not alter Eq. (11) and would modify Eq. (12) by adding a term of the form  $E_o \cdot \nabla (\nu_{in} n)$  to the right hand side (see also *Ossakow and Chaturvedi, 1978*). This would also alter Eq. (19), for example by changing it to

$$\gamma = \frac{1}{L} \left( \frac{g}{\nu_{in}} + \frac{cE_o}{B} \right) - \nu_R \quad (31)$$

where  $E_o$  is positive if in the eastward direction and negative if in the westward direction. Large enough values of a westward  $E_o$  could, depending on altitude of the F peak, result in stability. Any eastward  $E_o$  will make the instability grow faster. Similarly an eastward  $E_o$  will make the bubbles rise faster and a westward  $E_o$  will slow them down (see *Ossakow and Chaturvedi, 1978*). In any case, future studies including this effect and the effect of a horizontal neutral wind,  $V_n$ , (see *Ossakow and Chaturvedi, 1978*) are being planned.

Our present studies have been restrictive in the east-west ( $x$ ) dimension to bubble spatial sizes  $\sim 1$  km in this direction (total  $x$  dimension = 8 km). Our preliminary results from long wavelength ( $\sim 50$ -100 km) perturbation numerical simulations (Zalesak *et al.*, 1978) show that large transverse (east-west) bubble sizes may be generated by the nonlinear evolution of the collisional Rayleigh-Taylor instability: McClure *et al.* [1977] have also observed large transverse bubble dimensions. Future numerical simulation plans also include using random initial perturbations.

Our present numerical simulation studies as explicitly stated only covers the collisional Rayleigh-Taylor regime. This allows for the algebraic solution of the ion and electron momentum equations (see Eqs. (6) and (7)) and results in having to solve only two equations (Eqs. (11) and (12)) numerically. Including inertial effects and thus being able to handle the collisionless Rayleigh-Taylor regime requires solving the full two dimensional vector ion momentum equation (2) with the electrons still being described by Eq. (6). This is in addition to solving a continuity equation (1) and the divergence of the current equal to zero equation (8). Future plans call for making these changes. However, it should be pointed out that the range of validity of the collisional Rayleigh-Taylor regime requires  $\nu_{in}^2 > 4g/L$  (see for example Hudson and Kennel, 1975; Ossakow and Chaturvedi, 1978). Consequently, if we take  $L$  to be the bubble scale length, larger bubbles will remain in the collisional Rayleigh-Taylor regime to higher altitudes.

The physical picture of equatorial Spread F that emerges from our present simulation studies can be described as follows. After sunset the E region begins to recombine. Due to recombination and electrodynamic effects (or just recombination) the bottomside F region background electron density gradient begins to steepen. The electrodynamic effects are such that an eastward ambient electric field causes the bottomside density gradient to steepen and the F region to rise much akin to how a barium cloud would steepen and rise in equatorial

geometry (see *Ossakow and Chaturvedi, 1978*). Thus, the equatorial F region ionosphere can be viewed as a giant barium cloud (with inhomogeneities in the east-west direction occurring over very large spatial scale lengths). Indeed, our present studies of the nonlinear evolution of the collisional Rayleigh-Taylor instability are similar to our barium cloud striation studies (see *Scannapieco and Ossakow, 1976; Scannapieco et al., 1976*), except that the geometry has been rotated and gravity substitutes for an ambient electric field as the driving force. This steepening and rise can also be caused by a downward motion of the neutral atmosphere. When the altitude is high enough and/or bottomside background electron density gradients steep enough to overcome recombination effects density fluctuations will begin to grow (become linearly unstable) on the bottomside. If these altitude and gradient conditions are right plasma density depletions (bubbles) will form on the bottomside. Similarly, if these conditions are right these bubbles will then nonlinearly rise by polarization  $\mathbf{E} \times \mathbf{B}$  motion through the F peak and cause topside Spread F. Although the present series of simulations did not resolve meter size irregularities (in the present simulations  $\Delta y = 2$  km and  $\Delta x = 200$  meters), it is expected that the steepening bubbles, rising through the peak, will bifurcate (see for example *Ossakow et al, 1977*) on its topside and produce shorter and shorter wavelength irregularities either by a cascade or two step mechanism. For example, the gradients associated with the longer wavelength ( $\sim 100$  m-1 km) unstable fluid-type collisional Rayleigh-Taylor modes could result in shorter wavelength ( $\sim 1$  m) explosive growth kinetic instabilities.

Finally, we wish to compare our numerical simulation results with some of the experimental observations. The phenomenon of rising equatorial Spread F bubbles has been observed by rocket (*Kelley et al., 1976*) and satellite (*McClure et al., 1977*) in situ measurements and inferred from radar backscatter "plume" measurements (*Woodman and LaHoz, 1976*). The range of upward bubble velocities, depending on ambient ionospheric conditions, e.g. height of F peak and bottomside gradient scale length, in our simulations can account for many of the

experimental observations regarding the range of upward velocities reported by *McClure et al.* [1977]. To be sure a satellite is making a single point measurement and does not have all the background ionospheric driving conditions (coordinated measurements with ground based experiments and possibly rocket in situ measurements are needed). Nevertheless, the agreement between the simulations and the data (*McClure et al.*, 1977) is quite good. The dependence of the phenomena on high ionospheres, from the three meter backscatter results, has been noted by *Farley et al.* [1970] and *Woodman and La Hoz* [1976]. It should be pointed out that the 50 MHz (3 meter irregularities) backscatter is just a signature. Its full physical relation to the longer wavelength Rayleigh-Taylor modes, which can cause Spread F observed on ionograms and satellite transmission scintillation effects, is not unequivocally understood at this point. The long (in altitude) radar plume measurements (*Woodman and LaHoz*, 1976) could be related to the long bubbles (e.g., see ESF 3 and Fig. 9) connecting high and low altitudes (also see previous discussion in this section). The thin layer of bottomside irregularities observed by *Woodman and La Hoz* [1976] could be accounted for by having a low ionosphere, e.g., our numerical simulation results from ESF O and O'. Recently (August 1977), a coordinated equatorial F region measurement campaign was performed under the auspices of the Defense Nuclear Agency (DNA) at Kwajalein in the Marshall Islands. Some of the preliminary results from ionosonde (Drs. Bibl and Reinisch, University of Lowell), 1 meter (150 MHz) ALTAIR radar backscatter (Dr. Towle, MIT Lincoln Labs), and DNA Wideband, ATS-6 and Navy Transit satellite scintillation measurements (Drs. Baron, Tsunoda, Cousins and Livingston, SRI) agree with the results of the present numerical simulations, which depend on altitude of the F peak and steepness of the bottomside background electron density gradient.

#### **Acknowledgement**

We wish to thank Dr. A. J. Scannapieco for initially putting together the ESF numerical simulation code. This work was supported by the Defense Nuclear Agency and the Office of Naval Research.

### References

- Balsley, B.B., G. Haerendel and R.A. Greenwald, Equatorial Spread F: Recent observations and a new interpretation, *J. Geophys. Res.*, 77, 5625, 1972.
- Boris, J.P., and D.L. Book, Flux-corrected transport. I. SHASTA, a fluid transport algorithm that works, *J. Comp. Phys.* 11, 38, 1973.
- Chaturvedi, P.K., and P.K. Kaw, Steady state finite amplitude Rayleigh Taylor modes in Spread F, *Geophys. Res. Letts.*, 2, 381, 1975a.
- Chaturvedi, P.K., and P.K. Kaw, Correction, *Geophys. Res. Letts.*, 2, 499, 1975b.
- Chaturvedi, P., and P. Kaw, An interpretation for the power spectrum of Spread F irregularities, *J. Geophys. Res.* 81, 3257, 1976.
- Chaturvedi, P.K., and S.L. Ossakow, Nonlinear Theory of the collisional Rayleigh-Taylor instability in equatorial Spread F, *Geophys. Res. Letts.*, 4, 558, 1977.
- Costa, E., and M.C. Kelley, On the role of steepened structures and drift waves in equatorial Spread F, *J. Geophys. Res.* (submitted 1978a).
- Costa, E., and M.C. Kelley, Linear theory for the collisionless drift wave instability with wavelengths near the ion gyroradius, *J. Geophys. Res.* (submitted 1978b).
- Dyson, P.L., J. P. McClure and W.B. Hanson, In situ measurements of the spectral characteristics of F region ionospheric irregularities, *J. Geophys. Res.* 79, 1497, 1974.
- Farley, D.T., B.B. Balsley, R.F. Woodman, and J.P. McClure, Equatorial Spread F: Implications of VHF radar observations, *J. Geophys. Res.*, 75, 7199, 1970.
- Haerendel, G., Theory of Equatorial Spread F, preprint, Max-Planck Institute fur Physik und Astrophysik, 1974.
- Hudson, M.K., Spread F Bubbles: Nonlinear Rayleigh-Taylor mode in two dimensions, *J. Geophys. Res.* (to be published 1978).
- Hudson, M.K., and C.F. Kennel, Linear theory of equatorial Spread F, *J. Geophys. Res.*, 80, 4581, 1975.

- Kelley, M.C., G. Haerendel, H. Kappler, A. Valenzuela, B.B. Balsley, D.A. Carter, W.L. Ecklund, C.W. Carlson, B. Hausler, and R. Torbert, Evidence for a Rayleigh-Taylor type instability and upwelling of depleted density regions during equatorial spread F, *Geophys. Res. Letts.*, **3**, 448, 1976.
- Kelley, M.C., and E. Ott, Two-dimensional turbulence in equatorial Spread F, *J. Geophys. Res.* (submitted 1978).
- McClure, J.P., W.B. Hanson, and J.H. Hoffman, Plasma bubbles and irregularities in the equatorial ionosphere, *J. Geophys. Res.* **82**, 2650, 1977.
- McDonald, B.E., Explicit Chebychev-iterative solution of nonself-adjoint elliptic equations on a vector computer, NRL Memorandum Report 3541, June 1977.
- McFarland, M., D.L. Albritton, F.C. Fehsenfeld, E.E. Ferguson, and A.L. Schmeltekopf, Flow-drift technique for ion mobility and ion-molecule reaction rate constant measurements. II. Positive ion reactions of  $N^+$ ,  $O^+$  and  $N_2^+$  with  $O_2$  and  $O^+$  with  $N_2$  from thermal to  $\sim 2$  eV, *J. Chem. Phys.*, **59**, 6620, 1973.
- Morse, F.A., B.C. Edgar, H.C. Koons, C.J. Rice, W.J. Heikkila, J.H. Hoffman, B.A. Tinsley, J.D. Winningham, A.B. Christensen, R.F. Woodman, J. Pomalaza, and N.R. Teixeira, Equion, an equatorial ionospheric irregularity experiment, *J. Geophys. Res.*, **82**, 578, 1977.
- Ossakow, S.L., and P.K. Chaturvedi, Morphological studies of rising equatorial Spread F bubbles, *J. Geophys. Res.* (in press 1978).
- Ossakow, S.L., S.T. Zalesak, and N.J. Zabusky, Recent results on cleavage, bifurcation, and cascade mechanisms in ionospheric plasma clouds, NRL Memo Report 3579, August 1977.
- Ossakow, S.L., S.T. Zalesak, B.E. McDonald, and P.K. Chaturvedi, Theoretical and numerical simulation predictions of the equatorial Spread F environment, in *Proceedings of 1978 Symposium on the Effect of the Ionosphere on Space and Terrestrial Systems*, edited by J.M. Goodman, U.S. Government Printing Office, Washington, D.C., 1978.
- Ott, E., Theory of Rayleigh-Taylor bubbles in the equatorial ionosphere, *J. Geophys. Res.* (in

press 1978).

Scannapieco, A.J., and S.L. Ossakow, Nonlinear equatorial Spread F, *Geophys. Res. Letts.*, 3, 451, 1976.

Scannapieco, A.J., S.L. Ossakow, S.R. Goldman, and J.M. Pierre, Plasma cloud late time striation spectra, *J. Geophys. Res.*, 81, 6037, 1976.

Strobel, D.F., and M.B. McElroy, The F2-layer at middle latitudes, *Planet. Space Sci.*, 18, 1181, 1970.

Szuszczewicz, E.P., Ionospheric holes and equatorial spread F: chemistry and transport, *J. Geophys. Res.* (in press 1978).

Woodman, R.F. and C. La Hoz, Radar observations of F region equatorial irregularities, *J. Geophys. Res.* 81, 5447, 1976.

Zalesak, S.T., S.L. Ossakow, B.E. McDonald, and P.K. Chaturvedi, Numerical simulations of nonlinear equatorial Spread F, EOS, *Trans. Am. Geophys. Un.*, 58, 1202, 1977. Abstract.

Zalesak, S.T., S.L. Ossakow, B.E. McDonald, and P.K. Chaturvedi, Spatially large equatorial Spread F bubbles, *Trans. Am. Geophys. Un.*, 59, (1978 Spring Meeting, in press).

Table 1 — Numerical simulation cases considered.

ESF	Height of F peak, $h_p$ (km)	Minimum bottomside Scale length, L (km)
0	344	10
1	354	10
2	354	5
3	434	10

Table 2 — Results of Numerical Studies. Note the bubble rise velocity  $V_B$ , and the fractional depletion  $n_1/n_0$  refer to the values near the F peak altitude.

ESF	Altitude of F peak, $h_p$ (km)	Minimum bottomside Scale length, $L$ (km)	Bubble rise Velocity, $V_B$ (m/sec)	Percentage depletion $n_1/n_0$	Resulting Conditions
1	354	10	~12	~40%	Maximum linear growth rate $\gamma_M \sim 10^{-3} \text{ sec}^{-1}$ . Bottomside linear instability from 274 to 350 km altitude. Bubble passes peak ~ 8000 sec. Moderate top and bottomside Spread F with simulation stopped at $10^4$ sec.
2	354	5	~23	~60%	$\gamma_M \sim 3.2 \times 10^{-3} \text{ sec}^{-1}$ . Bottomside linear instability from 282 to 352 km altitude. Bubble passes peak ~ 4000 sec. Strong bottomside and moderate topside Spread F with simulation stopped at 5000 sec.
3	434	10	~160	~85%	$\gamma_M \sim 6 \times 10^{-3} \text{ sec}^{-1}$ . Entire bottomside from 332 to 434 km linearly unstable. Bubble passes peak ~ $10^3$ sec. Strong bottomside and topside Spread F with simulation stopped at 1400 sec.
0	344	10	~2.5	~16%	$\gamma_M \sim 6 \times 10^{-4} \text{ sec}^{-1}$ . Bottomside linearly unstable from 274 to 332 km. Bubble does not get to F peak rather dries up due to recombination. Weak bottomside Spread F only with simulation stopped at 15,000 sec.
O'	334	10	Undetermined	Undetermined	$\gamma_M \sim 2 \times 10^{-4} \text{ sec}^{-1}$ . Narrow bottomside region between 274 and 280 km linearly unstable. This would result in extremely weak bottomside Spread F. No nonlinear simulation performed.
O''	304	10	None	None	Entire bottomside between 202 and 304 km is linearly stable. No Spread F and no nonlinear simulation performed.

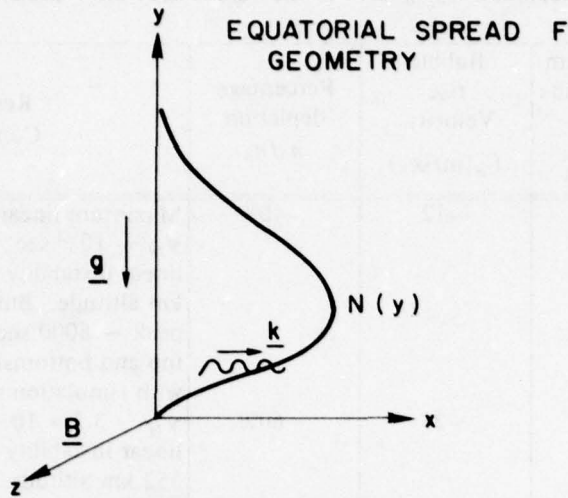


Fig. 1 - Equatorial Spread F geometry.  $N(y)$  represents the ambient electron density profile and has only altitude ( $y$ ) dependence.  $\underline{B}$  points to the north,  $x$  is west and so  $\underline{g} \times \underline{B}$  is to the east. A horizontal perturbation is denoted by  $\underline{k}$ .

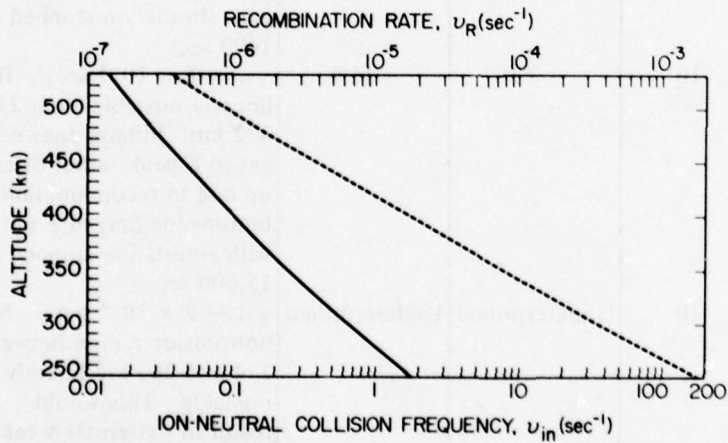


Fig. 2 - Ion-neutral collision frequency (solid line),  $\nu_{in}$ , and recombination rate (dashed line),  $\nu_R$ , as a function of altitude. The altitude range encompasses those altitudes used in the numerical simulations.

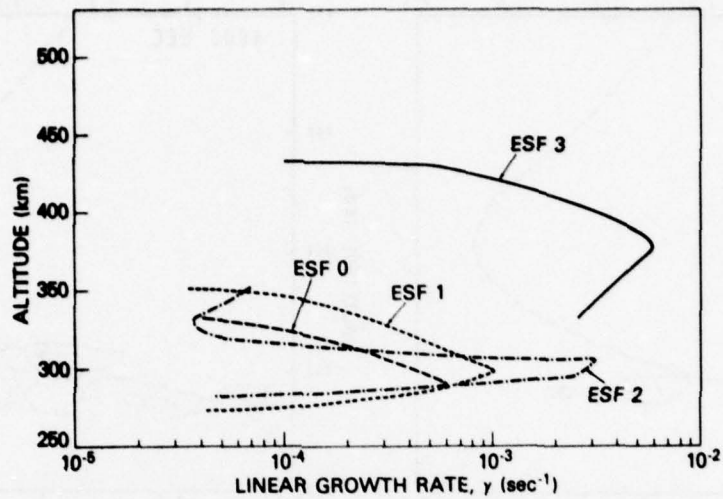


Fig. 3 - Linear growth rate,  $\gamma$ , versus altitude for the four numerical simulations ESF 0, ESF 1, 2, and 3 (see Table 1). A horizontal perturbation was assumed. Only the regions of instability are plotted for these four cases.

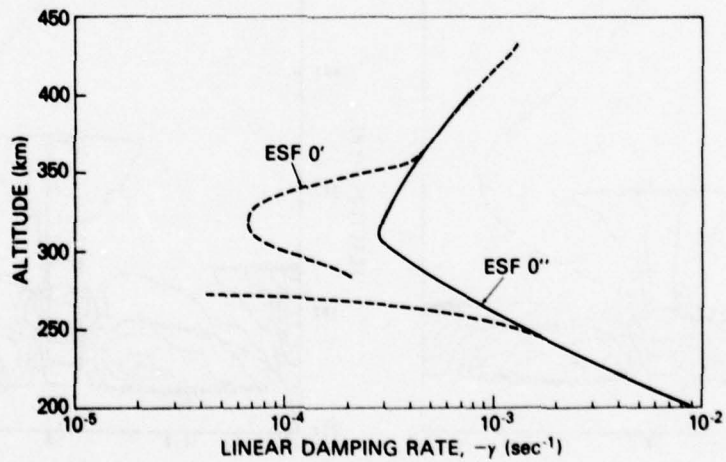


Fig. 4 - Linear damping rate,  $-\gamma$ , versus altitude for ESF O' and O''. ESF O' is the same shape as ESF 1 with the F peak moved down 20 km; similarly ESF O'' has the F peak moved down 50 km. A horizontal perturbation was assumed. Only the regions of stability have been plotted for these two cases.

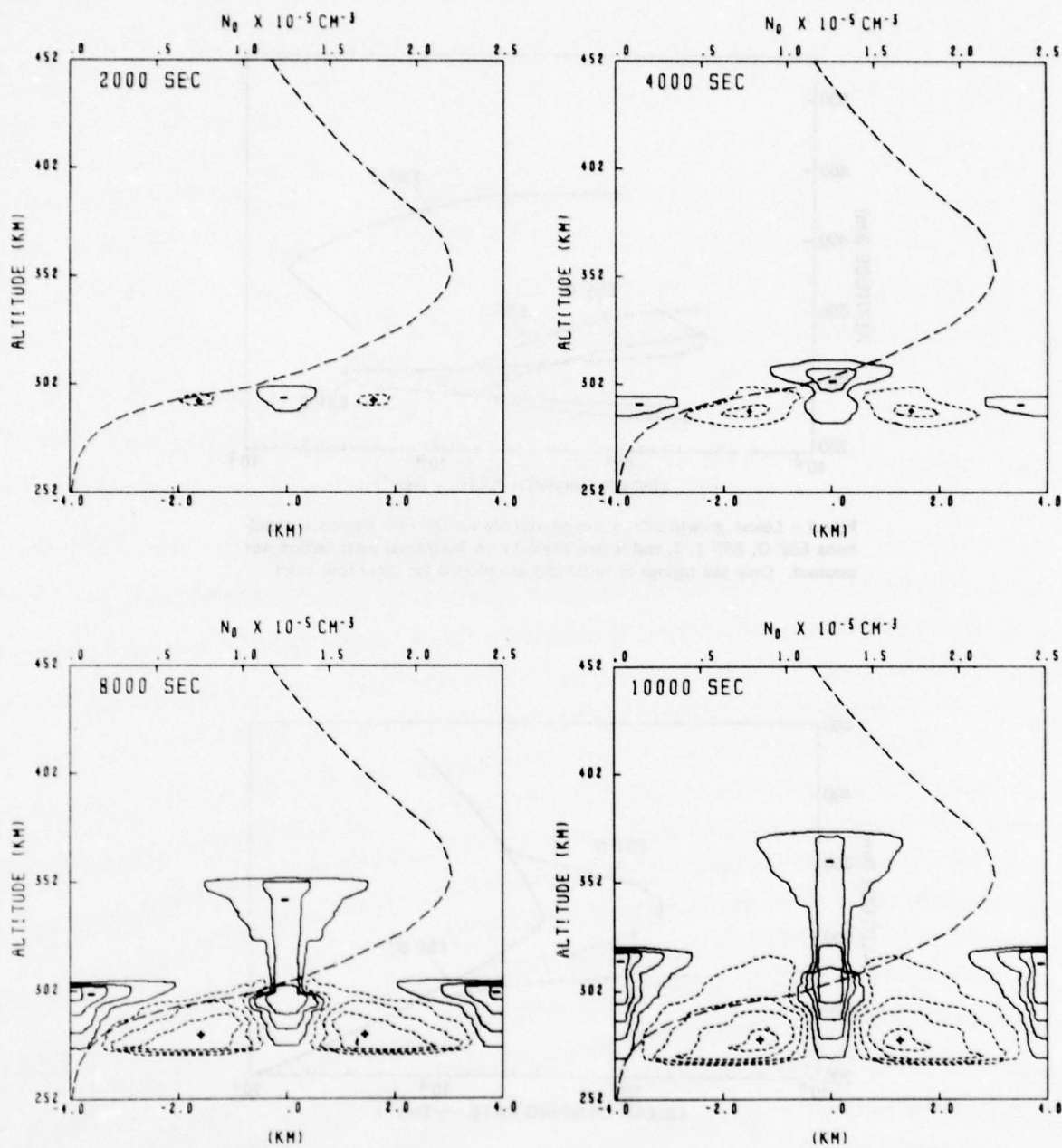


Fig. 5 - Contour plots of constant  $n_1/n_0$  for the simulation ESF 1 at  $t = 2000, 4000, 8000,$  and  $10,000$  sec. The small dashed contours with a plus sign inside and the solid contours with a minus sign inside indicate enhancement and depletions over the ambient electron number density. The large dashed curve depicts the ambient electron number density (values on upper horizontal axis),  $n_0$ , as a function of altitude. The vertical  $y$  axis represents altitude, the lower horizontal  $x$  axis is east-west range, and the ambient magnetic field is along the  $z$  axis, out of the figure.

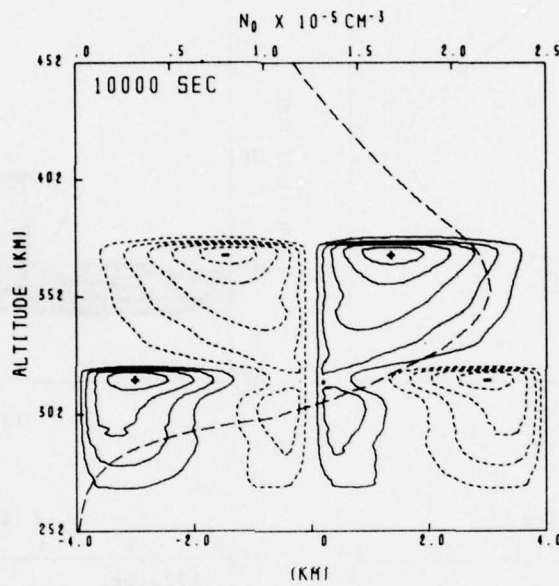


Fig. 6 - Contours of constant induced (polarization) potential,  $\phi_1$ , over the ESF 1 mesh (see Fig. 5) at  $t = 10,000$  sec. Plus and minus denote positive and negative values, with values decreasing in magnitude as one goes from the innermost to the outermost contours. The large dashed curve is  $n_0$ .

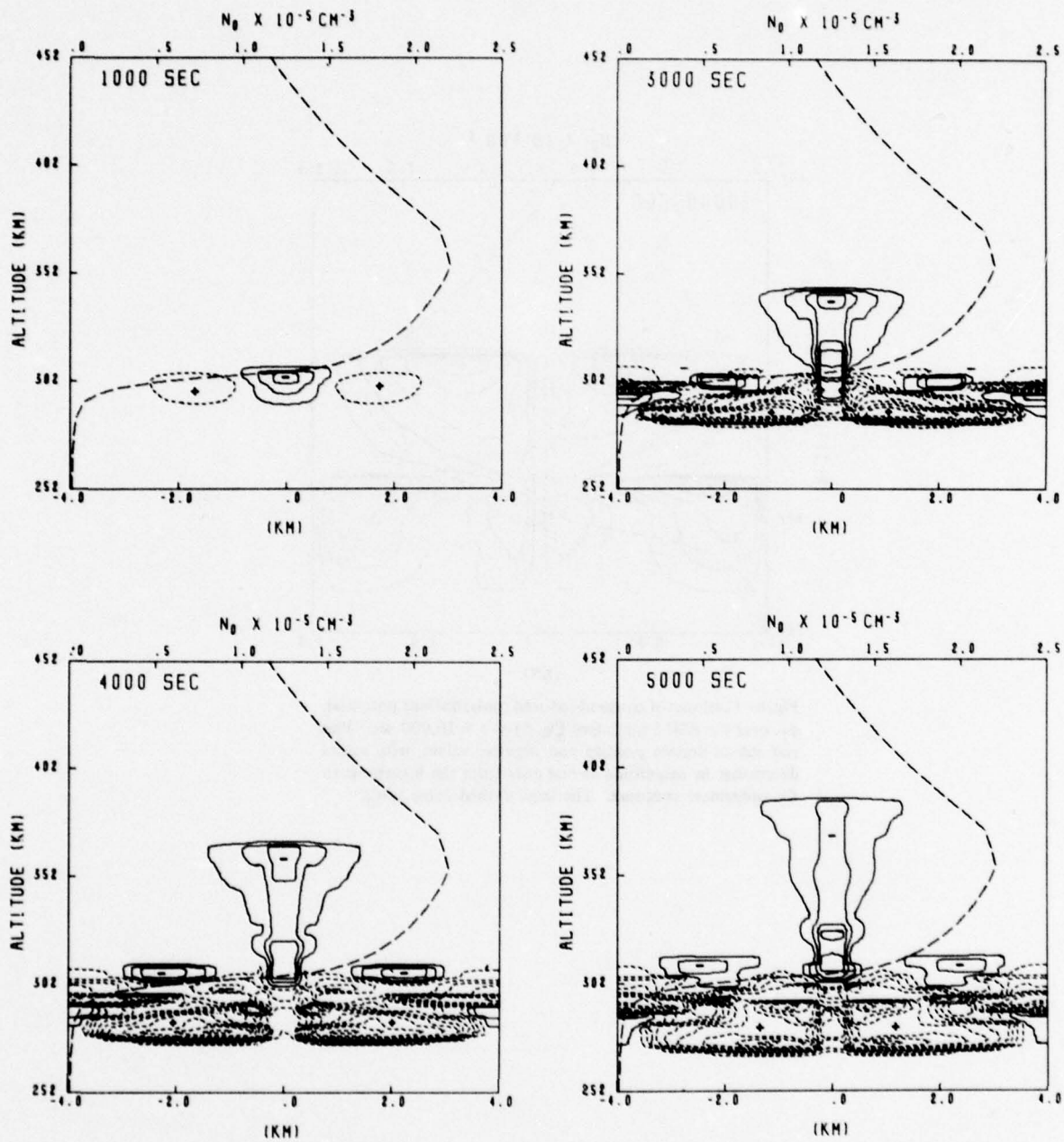


Fig. 7 - Contour plots of constant  $n_1/n_0$  for the ESF 2 simulation at  $t = 1000, 3000, 4000,$  and  $5000$  sec. All other nomenclature is the same as Fig. 5.

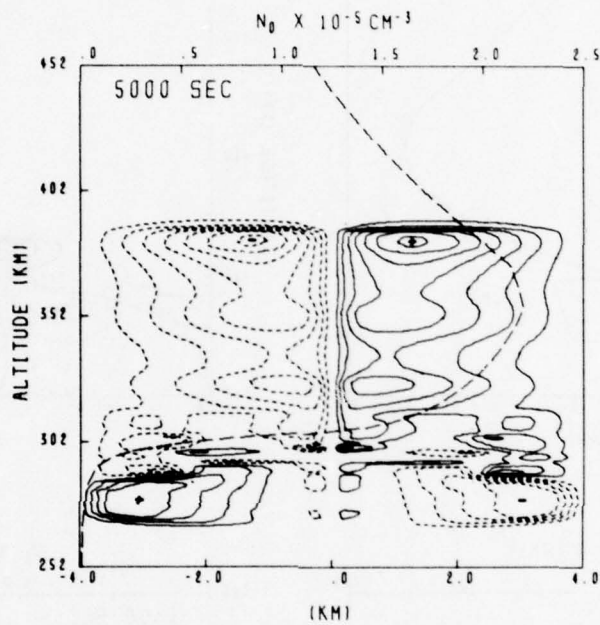


Fig. 8 - Contours of constant induced potential,  $\phi_1$ , over the ESF 2 mesh (see Fig. 7) at  $t = 5000$  sec. All other nomenclature is same as Fig. 6.

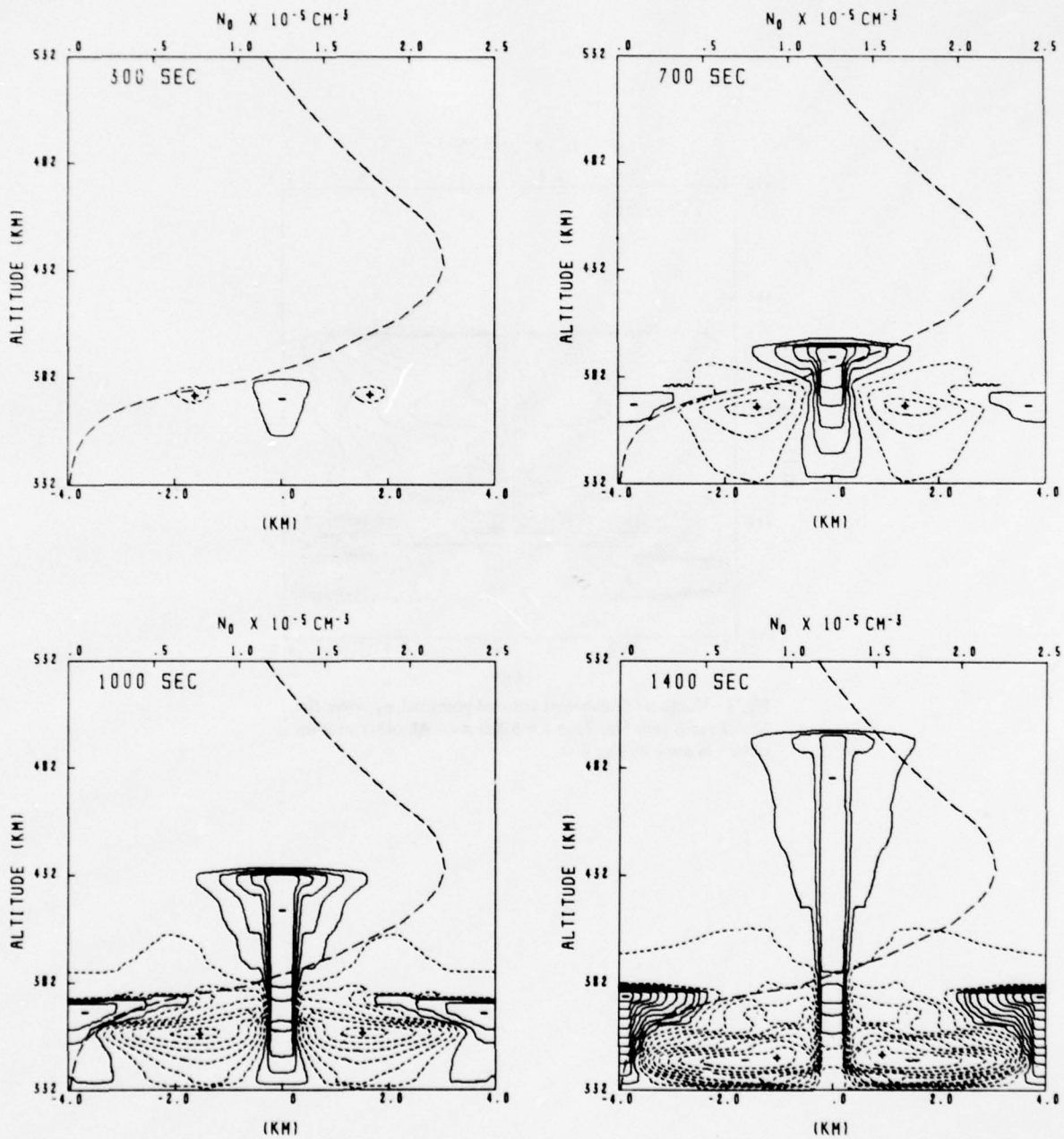


Fig. 9 - Contour plots of constant  $n_1/n_0$  for the ESF 3 simulation at  $t = 300, 700, 1000,$  and  $1400$  sec. All other nomenclature is same as Fig. 5.

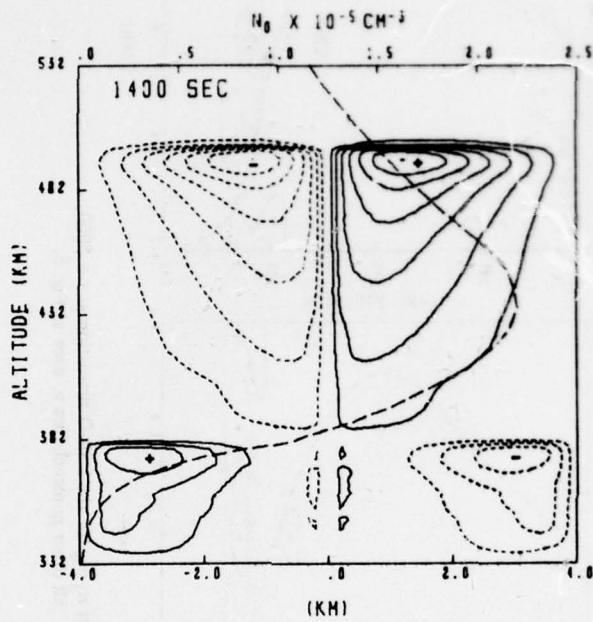


Fig. 10 - Contours of constant induced potential,  $\phi_1$ , over the ESF 3 mesh (see Fig. 9) at  $t = 1400$  sec. All other nomenclature is same as Fig. 6.

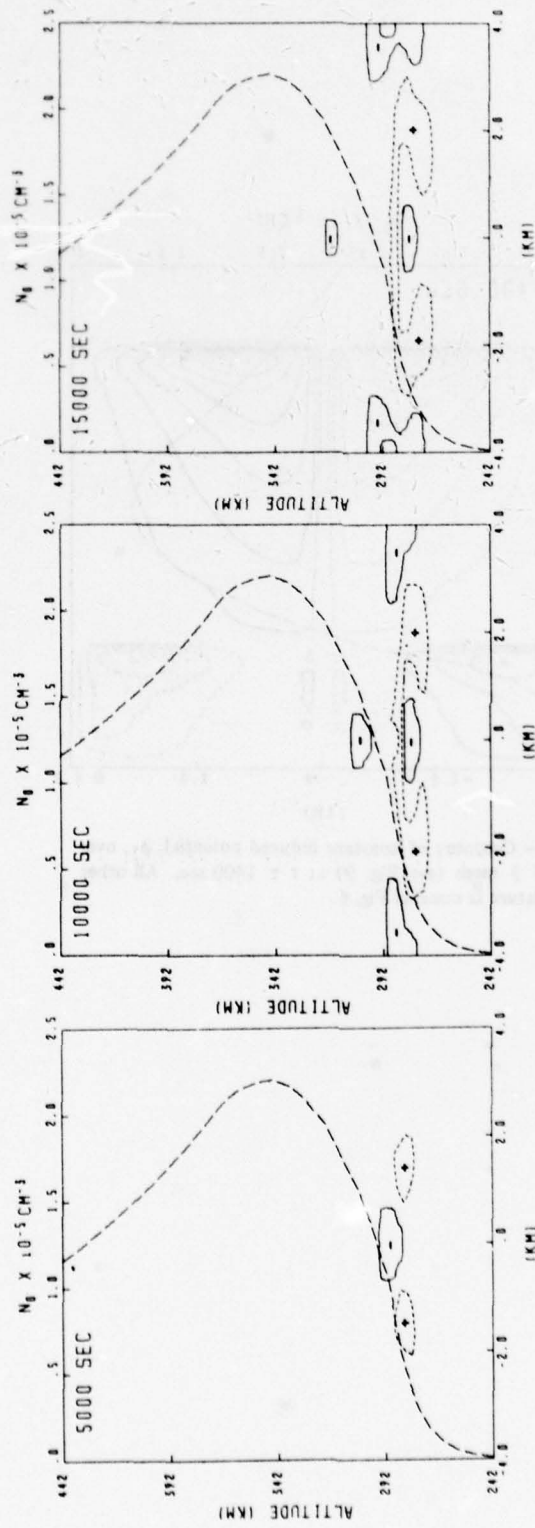


Fig. 11 - Contours of constant  $n_1/n_0$  for the ESF O simulation at  $t = 5000$ , 10,000, and 15,000 sec. All other nomenclature is same as Fig. 5.

DISTRIBUTION LIST

DEPARTMENT OF DEFENSE

ASSISTANT SECRETARY OF DEFENSE  
COMM, CMD, CONT & INTELL  
WASHINGTON, D.C. 20301

01CY ATTN J. BABCOCK  
01CY ATTN M. EPSTEIN

ASSISTANT TO THE SECRETARY OF DEFENSE  
ATOMIC ENERGY  
WASHINGTON, D.C. 20301

01CY ATTN EXECUTIVE ASSISTANT

DIRECTOR  
COMMAND CONTROL TECHNICAL CENTER  
PENTAGON RM BE 685  
WASHINGTON, D.C. 20301

01CY ATTN C-650  
01CY ATTN C-312 R. MASON

DIRECTOR  
DEFENSE ADVANCED RSCH PROJ AGENCY  
ARCHITECT BUILDING  
1400 WILSON BLVD.  
ARLINGTON, VA. 22209

01CY ATTN NUCLEAR MONITORING RESEARCH  
01CY ATTN STRATEGIC TECH OFFICE

DEFENSE COMMUNICATION ENGINEER CENTER  
1860 WIEHLE AVENUE  
RESTON, VA. 22090

01CY ATTN CODE R820  
01CY ATTN CODE R410 JAMES W. MCLEAN  
01CY ATTN CODE R720 J. WORTHINGTON

DIRECTOR  
DEFENSE COMMUNICATIONS AGENCY  
WASHINGTON, D.C. 20305

(ADR CNWDI: ATTN CODE 240 FOR)  
01CY ATTN CODE 480  
01CY ATTN CODE 810 R. W. ROSTRON  
01CY ATTN CODE 101B  
01CY ATTN CODE 103 M. RAFFENSPERGER

DEFENSE DOCUMENTATION CENTER  
CAMERON STATION  
ALEXANDRIA, VA. 22314

(12 COPIES IF OPEN PUBLICATION, OTHERWISE 2 COPIES)  
12CY ATTN TC

DIRECTOR  
DEFENSE INTELLIGENCE AGENCY  
WASHINGTON, D.C. 20301  
01CY ATTN DT-1B  
01CY ATTN DB-4C E. O'FARRELL  
01CY ATTN DIAAP A. WISE  
01CY ATTN DIAST-5  
01CY ATTN DT-1BZ R. MORTON  
01CY ATTN HQ-TR J. STEWART  
01CY ATTN W. WITTIG DC-7D

DIRECTOR  
DEFENSE NUCLEAR AGENCY  
WASHINGTON, D.C. 20305  
01CY ATTN STVL  
04CY ATTN TITL  
01CY ATTN DDST  
03CY ATTN RAAE

COMMANDER  
FIELD COMMAND  
DEFENSE NUCLEAR AGENCY  
KIRTLAND AFB, NM 87115  
01CY ATTN FCPR

DIRECTOR  
INTERSERVICE NUCLEAR WEAPONS SCHOOL  
KIRTLAND AFB, NM 87115  
01CY ATTN DOCUMENT CONTROL

JOINT CHIEFS OF STAFF  
WASHINGTON, D.C. 20301  
01CY ATTN J-3 WWMCCS EVALUATION OFFICE

DIRECTOR  
JOINT STRAT TGT PLANNING STAFF  
OFFUTT AFB  
OMAHA, NB 68113  
01CY ATTN JLTW-2  
01CY ATTN JPST G. GOETZ

CHIEF  
LIVERMORE DIVISION FLD COMMAND DNA  
DEPARTMENT OF DEFENSE  
LAWRENCE LIVERMORE LABORATORY  
P. O. BOX 808  
LIVERMORE, CA 94550  
01CY ATTN FCPR

DIRECTOR  
NATIONAL SECURITY AGENCY  
DEPARTMENT OF DEFENSE  
FT. GEORGE G. MEADE, MD 20755  
01CY ATTN JOHN SKILLMAN R52  
01CY ATTN FRANK LEONARD  
01CY ATTN W14 PAT CLARK  
01CY ATTN OLIVER H. BARTLETT W32  
01CY ATTN R5

COMMANDANT  
NATO SCHOOL (SHAPE)  
APO NEW YORK 09172  
01CY ATTN U.S. DOCUMENTS OFFICER

UNDER SECY OF DEF FOR RSCH & ENGRG  
DEPARTMENT OF DEFENSE  
WASHINGTON, D.C. 20301  
01CY ATTN STRATEGIC & SPACE SYSTEMS (OS)

WWMCCS SYSTEM ENGINEERING ORG  
WASHINGTON, D.C. 20305  
01CY ATTN R. CRAWFORD

COMMANDER/DIRECTOR  
ATMOSPHERIC SCIENCES LABORATORY  
U.S. ARMY ELECTRONICS COMMAND  
WHITE SANDS MISSILE RANGE, NM 88002  
01CY ATTN DELAS-EO F. NILES

DIRECTOR  
BMD ADVANCED TECH CTR  
HUNTSVILLE OFFICE  
P. O. BOX 1500  
HUNTSVILLE, AL 35807  
01CY ATTN ATC-T MELVIN T. CAPPS  
01CY ATTN ATC-O W. DAVIES  
01CY ATTN ATC-R DON RUSS

PROGRAM MANAGER  
BMD PROGRAM OFFICE  
5001 EISENHOWER AVENUE  
ALEXANDRIA, VA 22333  
01CY ATTN DACS-BMT J. SHEA

CHIEF C-E SERVICES DIVISION  
U.S. ARMY COMMUNICATIONS CMD  
PENTAGON RM 1B269  
WASHINGTON, D.C. 20310  
01CY ATTN C-E-SERVICES DIVISION

COMMANDER  
FRADCOM TECHNICAL SUPPORT ACTIVITY  
DEPARTMENT OF THE ARMY  
FORT MONMOUTH, N.J. 07703  
01CY ATTN DRSEL-NL-RD H. BENNET  
01CY ATTN DRSEL-PL-ENV H. BOMKE  
01CY ATTN J. E. QUIGLEY

COMMANDER  
HARRY DIAMOND LABORATORIES  
DEPARTMENT OF THE ARMY  
2800 POWDER MILL ROAD  
ADELPHI, MD 20783  
(CNWDI-INNER ENVELOPE: ATTN: DELHD-RBH)  
01CY ATTN DELHD-TI M. WEINER  
01CY ATTN DELHD-RB R. WILLIAMS  
01CY ATTN DELHD-NP F. WIMENITZ  
01CY ATTN DELHD-NP C. MOAZED

COMMANDER  
U.S. ARMY COMM-ELEC ENGRG INSTAL AGY  
FT. HUACHUCA, AZ 85613

01CY ATTN CCC-EMEO GEORGE LANE

COMMANDER  
U.S. ARMY FOREIGN SCIENCE & TECH CTR  
220 7TH STREET, NE  
CHARLOTTESVILLE, VA 22901  
01CY ATTN DRXST-SD  
01CY ATTN R. JONES

COMMANDER  
U.S. ARMY MATERIEL DEV & READINESS CMD  
5001 EISENHOWER AVENUE  
ALEXANDRIA, VA 22333  
01CY ATTN DRCLDC J. A. BENDER

COMMANDER  
U.S. ARMY NUCLEAR AND CHEMICAL AGENCY  
7500 BACKLICK ROAD  
BLDG 2073  
SPRINGFIELD, VA 22150  
01CY ATTN LIBRARY

DIRECTOR  
U.S. ARMY BALLISTIC RESEARCH LABS  
ABERDEEN PROVING GROUND, MD 21005  
01CY ATTN TECH LIB EDWARD BAICY

COMMANDER  
U.S. ARMY SATCOM AGENCY  
FT. MONMOUTH, NJ 07703  
01CY ATTN DOCUMENT CONTROL

COMMANDER  
U.S. ARMY MISSILE INTELLIGENCE AGENCY  
REDSTONE ARSENAL, AL 35809  
01CY ATTN JIM GAMBLE

DIRECTOR  
U.S. ARMY TRADOC SYSTEMS ANALYSIS ACTIVITY  
WHITE SANDS MISSILE RANGE, NM 88002  
01CY ATTN ATAA-SA  
01CY ATTN TCC/F. PAYAN JR.  
01CY ATTN ATAA-TAC LTC J. HESSE

COMMANDER  
NAVAL ELECTRONIC SYSTEMS COMMAND  
WASHINGTON, D.C. 20360  
01CY ATTN NAVALEX 034 T. HUGHES  
01CY ATTN PME 117  
01CY ATTN PME 117-T  
01CY ATTN CODE 5011

COMMANDING OFFICER  
NAVAL INTELLIGENCE SUPPORT CTR  
4301 SUITLAND ROAD, BLDG. 5  
WASHINGTON, D.C. 20390  
01CY ATTN MR. DUBBIN STIC 12  
01CY ATTN NISC-50  
01CY ATTN CODE 5404 J. GALET

COMMANDER

NAVAL OCEAN SYSTEMS CENTER  
SAN DIEGO, CA 92152

03CY ATTN CODE 532 W. MOLER  
01CY ATTN CODE 0230 C. BAGGETT  
01CY ATTN CODE 81 R. EASTMAN

DIRECTOR

NAVAL RESEARCH LABORATORY  
WASHINGTON, D.C. 20375

01CY ATTN CODE 6700 TIMOTHY P. COFFEY (25 CYS IF UNCLASS, 1 CY IF CLASS)  
01CY ATTN CODE 6701 JACK D. BROWN  
01CY ATTN CODE 6780 BRANCH HEAD (150 CYS IF UNCLASS, 1 CY IF CLASS)  
01CY ATTN CODE 7500 HQ COMM DIR BRUCE WALD  
01CY ATTN CODE 7550 J. DAVIS  
01CY ATTN CODE 7580  
01CY ATTN CODE 7551  
01CY ATTN CODE 7555  
01CY ATTN CODE 6730 E. MCLEAN  
01CY ATTN CODE 7127 C. JOHNSON

COMMANDER

NAVAL SEA SYSTEMS COMMAND  
WASHINGTON, D.C. 20362

01CY ATTN CAPT R. PITKIN

COMMANDER

NAVAL SPACE SURVEILLANCE SYSTEM  
DAHLGREN, VA 22448

01CY ATTN CAPT J. H. BURTON

OFFICER-IN-CHARGE

NAVAL SURFACE WEAPONS CENTER  
WHITE OAK, SILVER SPRING, MD 20910

01CY ATTN CODE F31

DIRECTOR

STRATEGIC SYSTEMS PROJECT OFFICE  
DEPARTMENT OF THE NAVY  
WASHINGTON, D.C. 20376

01CY ATTN NSP-2141  
01CY ATTN NSSP-2722 FRED WIMBERLY

NAVAL SPACE SYSTEM ACTIVITY

P. O. BOX 92960  
WORLDWAY POSTAL CENTER  
LOS ANGELES, CALIF. 90009

01CY ATTN A. B. HAZZARD

COMMANDER  
NAVAL SURFACE WEAPONS CENTER  
DAHLGREN LABORATORY  
DAHLGREN, VA 22448  
01CY ATTN CODE DF-14 R. BUTLER

COMMANDING OFFICER  
NAVY SPACE SYSTEMS ACTIVITY  
P.O. BOX 92960  
WORLDWAY POSTAL CENTER  
LOS ANGELES, CA. 90009  
01CY ATTN CODE 52

OFFICE OF NAVAL RESEARCH  
ARLINGTON, VA 22217  
01CY ATTN CODE 465  
01CY ATTN CODE 461  
01CY ATTN CODE 402  
01CY ATTN CODE 420  
01CY ATTN CODE 421

COMMANDER  
AEROSPACE DEFENSE COMMAND/DC  
DEPARTMENT OF THE AIR FORCE  
ENT AFB, CO 80912  
01CY ATTN DC MR. LONG

COMMANDER  
AEROSPACE DEFENSE COMMAND/XPD  
DEPARTMENT OF THE AIR FORCE  
ENT AFB, CO 80912  
01CY ATTN XPDQQ  
01CY ATTN XP

AIR FORCE GEOPHYSICS LABORATORY  
HANSCOM AFB, MA 01731  
01CY ATTN OPR HAROLD GARDNER  
01CY ATTN OPR-1 JAMES C. ULWICK  
01CY ATTN LKB KENNETH S. W. CHAMPION  
01CY ATTN OPR ALVA T. STAIR  
01CY ATTN PHP JULES AARONS  
01CY ATTN PHD JURGEN BUCHAU  
01CY ATTN PHD JOHN P. MULLEN

AF WEAPONS LABORATORY  
KIRTLAND AFB, NM 87117  
01CY ATTN SUL  
01CY ATTN CA ARTHUR H. GUENTHER  
01CY ATTN DYC CAPT J. BARRY  
01CY ATTN DYC JOHN M. KAMM  
01CY ATTN DYT CAPT MARK A. FRY  
01CY ATTN DES MAJ GARY GANONG  
01CY ATTN DYC J. JANNI

AFTAC  
PATRICK AFB, FL 32925  
01CY ATTN TF/MAJ WILEY  
01CY ATTN TN

AIR FORCE AVIONICS LABORATORY  
WRIGHT-PATTERSON AFB, OH 45433  
01CY ATTN AAD WADE HUNT  
01CY ATTN AAD ALLEN JOHNSON

DEPUTY CHIEF OF STAFF  
RESEARCH, DEVELOPMENT, & ACQ  
DEPARTMENT OF THE AIR FORCE  
WASHINGTON, D.C. 20330  
01CY ATTN AFRDQ

HEADQUARTERS  
ELECTRONIC SYSTEMS DIVISION/XR  
DEPARTMENT OF THE AIR FORCE  
HANSCOM AFB, MA 01731  
01CY ATTN XR J. DEAS

HEADQUARTERS  
ELECTRONIC SYSTEMS DIVISION/YSEA  
DEPARTMENT OF THE AIR FORCE  
HANSCOM AFB, MA 01731  
01CY ATTN YSEA

HEADQUARTERS  
ELECTRONIC SYSTEMS DIVISION/DC  
DEPARTMENT OF THE AIR FORCE  
HANSCOM AFB, MA 01731  
01CY ATTN DCKC MAJ J. C. CLARK

HEADQUARTERS  
ELECTRONIC SYSTEMS DIVISION, AFSC  
HANSCOM AFB, MA 01731  
01CY ATTN XRW  
01CY ATTN JAMES WHELAN

COMMANDER  
FOREIGN TECHNOLOGY DIVISION, AFSC  
WRIGHT-PATTERSON AFB, OH 45433  
01CY ATTN NICD LIBRARY  
01CY ATTN ETD P. BALLARD

COMMANDER  
ROME AIR DEVELOPMENT CENTER, AFSC  
GRIFFISS AFB, NY 13441  
01CY ATTN DOC LIBRARY/TSLD  
01CY ATTN UCSE V. COYNE

SAMSO/SZ  
POST OFFICE BOX 92960  
WORLDWAY POSTAL CENTER  
LOS ANGELES, CA 90009  
(SPACE DEFENSE SYSTEMS)  
01CY ATTN SZJ

STRATEGIC AIR COMMAND/XPFS  
OFFUTT AFB, NB 68113  
01CY ATTN XPFS MAJ B. STEPHAN  
01CY ATTN ADWATE MAJ BRUCE BAUER  
01CY ATTN NRT  
01CY ATTN DOK CHIEF SCIENTIST

SAMSO/YA  
P. O. BOX 92960  
WORLDWAY POSTAL CENTER  
LOS ANGELES, CA 90009  
01CY ATTN YAT CAPT L. BLACKWELDER

SAMSO/SK  
P. O. BOX 92960  
WORLDWAY POSTAL CENTER  
LOS ANGELES, CA 90009  
01CY ATTN SKA (SPACE COMM SYSTEMS) M. CLAVIN

SAMSO/MN  
NORTON AFB, CA 92409  
(MINUTEMAN)  
01CY ATTN MNL LTC KENNEDY

COMMANDER  
ROME AIR DEVELOPMENT CENTER, AFSC  
HANSCOM AFB, MA 01731  
01CY ATTN EEP A. LORENTZEN

DEPARTMENT OF ENERGY

DEPARTMENT OF ENERGY  
ALBUQUERQUE OPERATIONS OFFICE  
P. O. BOX 5400  
ALBUQUERQUE, NM 87115  
01CY ATTN DOC CON FOR D. SHERWOOD

DEPARTMENT OF ENERGY  
LIBRARY ROOM G-042  
WASHINGTON, D.C. 20545  
01CY ATTN DOC CON FOR A. LABOWITZ

EG&G, INC.  
LOS ALAMOS DIVISION  
P. O. BOX 809  
LOS ALAMOS, NM 85544  
01CY ATTN DOC CON FOR J. BREEDLOVE

UNIVERSITY OF CALIFORNIA  
LAWRENCE LIVERMORE LABORATORY  
P. O. BOX 808  
LIVERMORE, CA 94550  
01CY ATTN DOC CON FOR TECH INFO DEPT  
01CY ATTN DOC CON FOR L-389 R. OTT  
01CY ATTN DOC CON FOR L-31 R. HAGER  
01CY ATTN DOC CON FOR L-46 F. SEWARD

LOS ALAMOS SCIENTIFIC LABORATORY  
P. O. BOX 1663  
LOS ALAMOS, NM 87545  
01CY ATTN DOC CON FOR J. WOLCOTT  
01CY ATTN DOC CON FOR R. F. TASCHEK  
01CY ATTN DOC CON FOR E. JONES  
01CY ATTN DOC CON FOR J. MALIK  
01CY ATTN DOC CON FOR R. JEFFRIES  
01CY ATTN DOC CON FOR J. ZINN  
01CY ATTN DOC CON FOR P. KEATON  
01CY ATTN DOC CON FOR D. WESTERVELT

SANDIA LABORATORIES  
P. O. BOX 5800  
ALBUQUERQUE, NM 87115  
01CY ATTN DOC CON FOR J. MARTIN  
01CY ATTN DOC CON FOR W. BROWN  
01CY ATTN DOC CON FOR A. THORNBROUGH  
01CY ATTN DOC CON FOR T. WRIGHT  
01CY ATTN DOC CON FOR D. DAHLGREN  
01CY ATTN DOC CON FOR 3141  
01CY ATTN DOC CON FOR SPACE PROJECT DIV

SANDIA LABORATORIES  
LIVERMORE LABORATORY  
P. O. BOX 969  
LIVERMORE, CA 94550  
01CY ATTN DOC CON FOR B. MURPHEY  
01CY ATTN DOC CON FOR T. COOK

OFFICE OF MILITARY APPLICATION  
DEPARTMENT OF ENERGY  
WASHINGTON, D.C. 20545  
01CY ATTN DOC CON FOR D. GALE

OTHER GOVERNMENT

CENTRAL INTELLIGENCE AGENCY  
ATTN RD/SI, RM 5G48, HQ BLDG  
WASHINGTON, D.C. 20505  
01CY ATTN OSI/PSID RM 5F 19

DEPARTMENT OF COMMERCE  
NATIONAL BUREAU OF STANDARDS  
WASHINGTON, D.C. 20234  
(ALL CORRES: ATTN SEC OFFICER FOR)  
01CY ATTN R. MOORE

DEPARTMENT OF TRANSPORTATION  
OFFICE OF THE SECRETARY  
TAD-44.1, ROOM 10402-B  
400 7TH STREET, S.W.  
WASHINGTON, D.C. 20590  
01CY ATTN R. LEWIS  
01CY ATTN R. DOHERTY

INSTITUTE FOR TELECOM SCIENCES  
NATIONAL TELECOMMUNICATIONS & INFO ADMIN  
BOULDER, CO 80303  
01CY ATTN A. JEAN (UNCLASS ONLY)  
01CY ATTN W. UTLAUT  
01CY ATTN D. CROMBIE  
01CY ATTN L. BERRY

NATIONAL OCEANIC & ATMOSPHERIC ADMIN  
ENVIRONMENTAL RESEARCH LABORATORIES  
DEPARTMENT OF COMMERCE  
BOULDER, CO 80302  
01CY ATTN R. GRUBB  
01CY ATTN AERONOMY LAB G. REID

NASA  
GODDARD SPACE FLIGHT CENTER  
GREENBELT, MD 20771  
01CY ATTN P. CORRIGAN

DEPARTMENT OF DEFENSE CONTRACTORS

AEROSPACE CORPORATION

P. O. BOX 92957

LOS ANGELES, CA 90009

01CY ATTN I. GARFUNKEL

01CY ATTN T. SALMI

01CY ATTN V. JOSEPHSON

01CY ATTN S. BOWER

01CY ATTN N. STOCKWELL

01CY ATTN D. OLSEN

01CY ATTN J. CARTER

01CY ATTN F. MORSE

01CY ATTN SMFA FOR PWW

ANALYTICAL SYSTEMS ENGINEERING CORP

5 OLD CONCORD ROAD

BURLINGTON, MA 01803

01CY ATTN RADIO SCIENCES

BERKELEY RESEARCH ASSOCIATES, INC.

P. O. BOX 983

BERKELEY, CA 94701

01CY ATTN J. WORKMAN

BOEING COMPANY, THE

P. O. BOX 3707

SEATTLE, WA 98124

01CY ATTN G. KEISTER

01CY ATTN D. MURRAY

01CY ATTN G. HALL

01CY ATTN J. KENNEY

CALIFORNIA AT SAN DIEGO, UNIV OF

IPAPS, B-019

LA JOLLA, CA 92093

01CY ATTN HENRY G. BOOKER

BROWN ENGINEERING COMPANY, INC.

CUMMINGS RESEARCH PARK

HUNTSVILLE, AL 35807

01CY ATTN ROMEO A. DELIBERIS

CHARLES STARK DRAPER LABORATORY, INC.

555 TECHNOLOGY SQUARE

CAMBRIDGE, MA 02139

01CY ATTN D. B. COX

01CY ATTN J. P. GILMORE

COMPUTER SCIENCES CORPORATION

6565 ARLINGTON BLVD

FALLS CHURCH, VA 22046

01CY ATTN H. BLANK

01CY ATTN JOHN SPOOR

01CY ATTN C. NAIL

COMSAT LABORATORIES  
LINTHICUM ROAD  
CLARKSBURG, MD 20734  
01CY ATTN G. HYDE

CORNELL UNIVERSITY  
DEPARTMENT OF ELECTRICAL ENGINEERING  
ITHACA, NY 14850  
01CY ATTN D. T. FARLEY JR

ELECTROSPACE SYSTEMS, INC.  
BOX 1359  
RICHARDSON, TX 75080  
01CY ATTN H. LOGSTON  
01CY ATTN SECURITY (PAUL PHILLIPS)

ESL INC.  
495 JAVA DRIVE  
SUNNYVALE, CA 94086  
01CY ATTN J. ROBERTS  
01CY ATTN JAMES MARSHALL  
01CY ATTN C. W. PRETTIE

FORD AEROSPACE & COMMUNICATIONS CORP  
3939 FABIAN WAY  
PALO ALTO, CA 94303  
01CY ATTN J. T. MATTINGLEY

GENERAL ELECTRIC COMPANY  
SPACE DIVISION  
VALLEY FORGE SPACE CENTER  
GODDARD BLVD KING OF PRUSSIA  
P. O. BOX 8555  
PHILADELPHIA, PA 19101  
01CY ATTN M. H. BORTNER SPACE SCI LAB

GENERAL ELECTRIC COMPANY  
P. O. BOX 1122  
SYRACUSE, NY 13201  
01CY ATTN F. REIBERT

GENERAL ELECTRIC COMPANY  
TEMPO-CENTER FOR ADVANCED STUDIES  
816 STATE STREET (P.O. DRAWER QQ)  
SANTA BARBARA, CA 93102  
01CY ATTN DASIAC  
01CY ATTN DON CHANDLER  
01CY ATTN TOM BARRETT  
01CY ATTN TIM STEPHANS  
01CY ATTN WARREN S. KNAPP  
01CY ATTN WILLIAM MCNAMARA  
01CY ATTN B. GAMBILL  
01CY ATTN MACK STANTON

GENERAL ELECTRIC TECH SERVICES CO., INC.  
HMES  
COURT STREET  
SYRACUSE, NY 13201  
01CY ATTN G. MILLMAN

GENERAL RESEARCH CORPORATION  
SANTA BARBARA DIVISION  
P. O. BOX 6770  
SANTA BARBARA, CA 93111  
01CY ATTN JOHN ISE JR  
01CY ATTN JOEL GARBARINO

GEOPHYSICAL INSTITUTE  
UNIVERSITY OF ALASKA  
FAIRBANKS, AK 99701  
(ALL CLASS ATTN: SECURITY OFFICER)  
01CY ATTN T. N. DAVIS (UNCL ONLY)  
01CY ATTN NEAL BROWN (UNCL ONLY)  
01CY ATTN TECHNICAL LIBRARY

GTE SYLVANIA, INC.  
ELECTRONICS SYSTEMS GRP-EASTERN DIV  
77 A STREET  
NEEDHAM, MA 02194  
01CY ATTN MARSHAL CROSS

ILLINOIS, UNIVERSITY OF  
DEPARTMENT OF ELECTRICAL ENGINEERING  
URBANA, IL 61803  
01CY ATTN K. YEH

ILLINOIS, UNIVERSITY OF  
107 COBLE HALL  
801 S. WRIGHT STREET  
URBANA, IL 60680  
(ALL CORRES ATTN SECURITY SUPERVISOR FOR)  
01CY ATTN K. YEH

INSTITUTE FOR DEFENSE ANALYSES  
400 ARMY-NAVY DRIVE  
ARLINGTON, VA 22202  
01CY ATTN J. M. AEIN  
01CY ATTN ERNEST BAUER  
01CY ATTN HANS WOLFHARD  
01CY ATTN JOEL BENGSTON

HSS, INC.  
2 ALFRED CIRCLE  
BEDFORD, MA 01730  
01CY ATTN DONALD HANSEN

INTL TEL & TELEGRAPH CORPORATION  
500 WASHINGTON AVENUE  
NUTLEY, NJ 07110  
01CY ATTN TECHNICAL LIBRARY

JAYCOR  
1401 CAMINO DEL MAR  
DEL MAR, CA 92014  
01CY ATTN S. R. GOLDMAN

JOHNS HOPKINS UNIVERSITY  
APPLIED PHYSICS LABORATORY  
JOHNS HOPKINS ROAD  
LAUREL, MD 20810

01CY ATTN DOCUMENT LIBRARIAN  
01CY ATTN THOMAS POTEMRA  
01CY ATTN JOHN DASSOULAS

LOCKHEED MISSILES & SPACE CO INC  
P. O. BOX 504  
SUNNYVALE, CA 94088

01CY ATTN DEPT 60-12  
01CY ATTN D. R. CHURCHILL

LOCKHEED MISSILES AND SPACE CO INC  
3251 HANOVER STREET  
PALO ALTO, CA 94304

01CY ATTN MARTIN WALT DEPT 52-10  
01CY ATTN RICHARD G. JOHNSON DEPT 52-12  
01CY ATTN W. L. IMHOF DEPT 52-12

KAMAN SCIENCES CORP  
P. O. BOX 7463  
COLORADO SPRINGS, CO 80933  
01CY ATTN T. MEAGHER

LINKABIT CORP  
10453 ROSELLE  
SAN DIEGO, CA 92121  
01CY ATTN IRWIN JACOBS

LOWELL RSCH FOUNDATION, UNIVERSITY OF  
450 AIKEN STREET  
LOWELL, MA 01854  
01CY ATTN K. BIBL

M.I.T. LINCOLN LABORATORY  
P. O. BOX 73  
LEXINGTON, MA 02173  
01CY ATTN DAVID M. TOWLE  
01CY ATTN P. WALDRON  
01CY ATTN L. LOUGHLIN  
01CY ATTN D. CLARK

MARTIN MARIETTA CORP  
ORLANDO DIVISION  
P. O. BOX 5837  
ORLANDO, FL 32805  
01CY ATTN R. HEFFNER

MCDONNELL DOUGLAS CORPORATION  
5301 BOLSA AVENUE  
HUNTINGTON BEACH, CA 92647  
01CY ATTN N. HARRIS  
01CY ATTN J. MOULE  
01CY ATTN GEORGE MROZ  
01CY ATTN W. OLSON  
01CY ATTN R. W. HALPRIN  
01CY ATTN TECHNICAL LIBRARY SERVICES

MISSION RESEARCH CORPORATION  
735 STATE STREET  
SANTA BARBARA, CA 93101

01CY ATTN P. FISCHER  
01CY ATTN W. F. CREVIER  
01CY ATTN STEVEN L. GUTSCHE  
01CY ATTN D. SAPPENFIELD  
01CY ATTN R. BOGUSCH  
01CY ATTN R. HENDRICK  
01CY ATTN RALPH KILB  
01CY ATTN DAVE SOWLE  
01CY ATTN F. FAJEN  
01CY ATTN M. SCHEIBE  
01CY ATTN CONRAD L. LONGMIRE  
01CY ATTN WARREN A. SCHLUETER

MITRE CORPORATION, THE  
P. O. BOX 208  
BEDFORD, MA 01730

01CY ATTN JOHN MORGANSTERN  
01CY ATTN G. HARDING  
01CY ATTN C. E. CALLAHAN

MITRE CORP  
WESTGATE RESEARCH PARK  
1820 DOLLY MADISON BLVD  
MCLEAN, VA 22101

01CY ATTN W. HALL  
01CY ATTN W. FOSTER

PACIFIC-SIERRA RESEARCH CORP  
1456 CLOVERFIELD BLVD.  
SANTA MONICA, CA 90404

01CY ATTN E. C. FIELD JR

PENNSYLVANIA STATE UNIVERSITY  
IONOSPHERE RESEARCH LAB  
318 ELECTRICAL ENGINEERING EAST  
UNIVERSITY PARK, PA 16802

(NO CLASSIFIED TO THIS ADDRESS)  
01CY ATTN IONOSPHERIC RESEARCH LAB

PHOTOMETRICS, INC.  
442 MARRETT ROAD  
LEXINGTON, MA 02173

01CY ATTN IRVING L. KOFKY

PHYSICAL DYNAMICS INC.  
P. O. BOX 3027  
BELLEVUE, WA 98009

01CY ATTN E. J. FREMOUW

PHYSICAL DYNAMICS INC.  
P. O. BOX 1069  
BERKELEY, CA 94701

01CY ATTN A. THOMPSON

R & D ASSOCIATES

P. O. BOX 9695

MARINA DEL REY, CA 90291

01CY ATTN FORREST GILMORE  
01CY ATTN BRYAN GABBARD  
01CY ATTN WILLIAM B. WRIGHT JR  
01CY ATTN ROBERT F. LELEVIER  
01CY ATTN WILLIAM J. KARZAS  
01CY ATTN H. ORY  
01CY ATTN C. MACDONALD  
01CY ATTN R. TURCO

RAND CORPORATION, THE

1700 MAIN STREET

SANTA MONICA, CA 90406

01CY ATTN CULLEN CRAIN  
01CY ATTN ED BEDROZIAN

RIVERSIDE RESEARCH INSTITUTE

80 WEST END AVENUE

NEW YORK, NY 10023

01CY ATTN VINCE TRAPANI

SCIENCE APPLICATIONS, INC.

P. O. BOX 2351

LA JOLLA, CA 92038

01CY ATTN LEWIS M. LINSON  
01CY ATTN DANIEL A. HAMLIN  
01CY ATTN D. SACHS  
01CY ATTN E. A. STRAKER  
01CY ATTN CURTIS A. SMITH  
01CY ATTN JACK MCDUGALL

RAYTHEON CO.

528 BOSTON POST ROAD

SUDBURY, MA 01776

01CY ATTN BARBARA ADAMS

SCIENCE APPLICATIONS, INC.

HUNTSVILLE DIVISION

2109 W. CLINTON AVENUE

SUITE 700

HUNTSVILLE, AL 35805

01CY ATTN DALE H. DIVIS

SCIENCE APPLICATIONS, INCORPORATED

8400 WESTPARK DRIVE

MCLEAN, VA 22101

01CY ATTN J. COCKAYNE

SCIENCE APPLICATIONS, INC.

80 MISSION DRIVE

PLEASANTON, CA 94566

01CY ATTN SZ

SRI INTERNATIONAL  
333 RAVENSWOOD AVENUE  
MENLO PARK, CA 94025

01CY ATTN DONALD NEILSON  
01CY ATTN ALAN BURNS  
01CY ATTN G. SMITH  
01CY ATTN L. L. COBB  
01CY ATTN DAVID A. JOHNSON  
01CY ATTN WALTER G. CHESNUT  
01CY ATTN CHARLES L. RINO  
01CY ATTN WALTER JAYE  
01CY ATTN M. BARON  
01CY ATTN RAY L. LEADABRAND  
01CY ATTN G. CARPENTER  
01CY ATTN G. PRICE  
01CY ATTN J. PETERSON  
01CY ATTN R. HAKE, JR.  
01CY ATTN V. GONZALES  
01CY ATTN D. MCDANIEL

TECHNOLOGY INTERNATIONAL CORP  
75 WIGGINS AVENUE  
BEDFORD, MA 01730

01CY ATTN W. P. BOQUIST

TRW DEFENSE & SPACE SYS GROUP  
ONE SPACE PARK  
REDONDO BEACH, CA 90278

01CY ATTN R. K. PLEBUCH  
01CY ATTN S. ALTSCHULER  
01CY ATTN D. DEE

VISIDYNE, INC.  
19 THIRD AVENUE  
NORTH WEST INDUSTRIAL PARK  
BURLINGTON, MA 01803

01CY ATTN CHARLES HUMPHREY  
01CY ATTN J. W. CARPENTER

IONOSPHERIC MODELING DISTRIBUTION LIST  
UNCLASSIFIED ONLY

PLEASE DISTRIBUTE ONE COPY TO EACH OF THE FOLLOWING PEOPLE:

ADVANCED RESEARCH PROJECTS AGENCY (ARPA)  
STRATEGIC TECHNOLOGY OFFICE  
ARLINGTON, VIRGINIA

CAPT. DONALD M. LEVINE

NAVAL RESEARCH LABORATORY  
WASHINGTON, D.C. 20375

DR. P. MANGE  
DR. R. MEIER  
DR. E. SZUSZCZEWICZ - CODE 7127  
DR. TIMOTHY COFFEY - CODE 6700  
DR. S. OSSAKOW - CODE 6780  
DR. J. GOODMAN - CODE 7560

SCIENCE APPLICATIONS, INC.  
1250 PROSPECT PLAZA  
LA JOLLA, CALIFORNIA 92037

DR. D. A. HAMLIN  
DR. L. LINSON  
DR. D. SACHS

DIRECTOR OF SPACE AND ENVIRONMENTAL LABORATORY  
NOAA  
BOULDER, COLORADO 80302

DR. A. GLENN JEAN  
DR. G. W. ADAMS  
DR. D. N. ANDERSON  
DR. K. DAVIES  
DR. R. F. DONNELLY

A. F. GEOPHYSICS LABORATORY  
L. G. HANSOM FIELD  
BEDFORD, MASS. 01730

DR. T. ELKINS  
DR. W. SWIDER  
MRS. R. SAGALYN  
DR. J. M. FORBES  
DR. T. J. KENESHEA  
DR. J. AARONS

OFFICE OF NAVAL RESEARCH  
800 NORTH QUINCY STREET  
ARLINGTON, VIRGINIA 22217

DR. H. MULLANEY

COMMANDER  
NAVAL ELECTRONICS LABORATORY CENTER  
SAN DIEGO, CALIFORNIA 92152

DR. M. BLEIWEISS  
DR. I. ROTHMULLER  
DR. V. HILDEBRAND  
MR. R. ROSE

U. S. ARMY ABERDEEN RESEARCH AND DEVELOPMENT CENTER  
BALLISTIC RESEARCH LABORATORY  
ABERDEEN, MARYLAND

DR. J. HEIMERL

COMMANDER  
NAVAL AIR SYSTEMS COMMAND  
DEPARTMENT OF THE NAVY  
WASHINGTON, D.C. 20360

DR. T. CZUBA

HARVARD UNIVERSITY  
HARVARD SQUARE  
CAMBRIDGE, MASS. 02138

DR. M. B. MCELROY  
DR. R. LINDZEN

PENNSYLVANIA STATE UNIVERSITY  
UNIVERSITY PARK, PENNSYLVANIA 16802

DR. J. S. NISBET  
DR. P. R. ROHRBAUGH  
DR. D. E. BARAN  
DR. L. A. CARPENTER  
DR. M. LEE  
DR. R. DIVANY  
DR. P. BENNETT  
DR. E. KLEVANS

UNIVERSITY OF CALIFORNIA, LOS ANGELES  
405 HILLGARD AVENUE  
LOS ANGELES, CALIFORNIA 90024

DR. F. V. CORONITI  
DR. C. KENNEL

UNIVERSITY OF CALIFORNIA, BERKELEY  
BERKELEY, CALIFORNIA 94720

DR. M. HUDSON

UTAH STATE UNIVERSITY  
4TH N. AND 8TH STREETS  
LOGAN, UTAH 84322

DR. P. M. BANKS  
DR. R. HARRIS  
DR. V. PETERSON  
DR. R. MEGILL  
DR. K. BAKER

CORNELL UNIVERSITY  
ITHACA, NEW YORK 14850

DR. W. E. SWARTZ  
DR. R. SUDAN  
DR. D. FARLEY  
DR. M. KELLEY  
DR. E. OTT

NASA  
GODDARD SPACE FLIGHT CENTER  
GREENBELT, MARYLAND 20771

DR. S. CHANDRA  
DR. K. MAEDO

PRINCETON UNIVERSITY  
PLASMA PHYSICS LABORATORY  
PRINCETON, NEW JERSEY 08540

DR. F. PERKINS  
DR. E. FRIEMAN

INSTITUTE FOR DEFENSE ANALYSIS  
400 ARMY/NAVY DRIVE  
ARLINGTON, VIRGINIA 22202

DR. E. BAUER

UNIVERSITY OF PITTSBURGH  
PITTSBURGH, PA. 15213

DR. N. ZABUSKY  
DR. M. BIONDI